



# Effect of interplanetary shock waves on turbulence parameters

Emilia Kilpua<sup>1</sup>, Simon Good<sup>1</sup>, Juska Soljento<sup>1</sup>, Domenico Trotta<sup>2</sup>, Tia Bäcker<sup>1</sup>, Julia Ruohotie<sup>1</sup>, Jens Pomoell<sup>1</sup>, Chaitanya Sishtla<sup>1,3</sup>, and Rami Vainio<sup>4</sup>

<sup>1</sup>Department of Physics, University of Helsinki, P.O. Box 64, FI-00014 Helsinki, Finland

<sup>2</sup>The Blackett Laboratory, Department of Physics, Imperial College London, London SW7 2AZ, UK

<sup>3</sup>Department of Physics and Astronomy, Queen Mary University of London, London E1 4NS, UK

<sup>4</sup>Department of Physics and Astronomy, University of Turku, FI-20014 Turku, Finland

**Correspondence:** Emilia Kilpua (emilia.kilpua@helsinki.fi)

**Abstract.** We have performed an extensive statistical investigation of how interplanetary fast forward shocks affect certain turbulence parameters – namely, the normalised cross-helicity ( $\sigma_c$ ), residual energy ( $\sigma_r$ ) and magnetic helicity ( $\sigma_m$ ). A total of 371 shocks detected by *Wind* at 1 au and seven shocks by *Solar Orbiter* below 0.5 au have been analysed. We explore how the aforementioned turbulence parameters and their variations across the shock depend on the shock characteristics, i.e. the gas compression ratio, upstream plasma beta, velocity jump and shock angle. We find that in the shock vicinity, fluctuations tend to show outward imbalance (measured by  $\sigma_c$ ), dominance of magnetic energy (negative  $\sigma_r$ ) and zero  $\sigma_m$  when averaged over longer periods. The tendency for imbalance and high Alfvénicity ( $\sigma_r \sim 0$ ) increases with increasing shock velocity jump, and decreasing upstream beta and shock angle. Shocks with large velocity jumps and gas compression ratio have considerably more balanced ( $\sigma_c \sim 0$ ) and less Alfvénic fluctuations in their downstream than upstream, presumably resulting both from Alfvénic fluctuations not passing to the downstream and generation of new compressive fluctuations. We also find that frequency of periods fulfilling the criteria for Alfvén fluctuations (AF) usually decreases, while those meeting the criteria for small-scale flux ropes (SFR) increases from upstream to downstream. The occurrence of AF-like periods peaks for quasi-parallel shocks with large velocity jump, and small upstream beta values. The occurrence of SFR in turn increases with increasing gas compression ratio and upstream beta. The shocks observed by *Solar Orbiter* at 0.3 – 0.5 au feature overall similar distributions of turbulence parameters and similar upstream-to-downstream changes as detected at 1 au. These results are relevant for understanding turbulence and charged-particle acceleration at collisionless shocks.

## 1 Introduction

The solar wind is a continuous flow of collisionless plasma from the Sun into interplanetary space (Parker, 1958). It is permeated by a variety of waves, structures and a turbulence cascade in which energy injected at large scales transfers through an intermediate inertial range to kinetic scales, where it finally dissipates (e.g., Bruno and Carbone, 2013; Verscharen et al., 2019). The dominant fluctuation modes in the solar wind are Alfvénic in nature (Belcher and Davis, 1971), exhibiting strong correlation or anti-correlation between the magnetic field and velocity vectors. Alfvénic fluctuations are particularly dominant in fast solar wind streams (e.g., Snekvik et al., 2013) but are also observed in the slow solar wind (e.g., D’Amicis et al., 2021).



The origin of the antisunward-propagating Alfvén waves seen at injection scales, which supply energy to the turbulent cascade  
25 at inertial scales, has been linked, for example, to convective motions in the photosphere, with the waves resulting from these  
motions being swept into interplanetary space with the solar wind outflow (e.g., Tomczyk and McIntosh, 2009; Cranmer and  
Van Ballegoijen, 2005).

Sunward propagating Alfvén waves may be generated by reflection of outward propagating waves in the stratified plasma  
and via non-linear processes such as the parametric decay instability (e.g., Goldstein, 1978; Gary, 2001; Sishtla et al., 2022),  
30 and also in regions where large velocity shears are present (e.g., Soljento et al., 2023). The sunward fluctuations below and  
above the critical point must in turn be generated in the sub-Alfvénic and super-Alfvénic solar wind, respectively.

An important question is how fast forward interplanetary shock waves affect the parameters that characterise solar wind  
fluctuations (e.g., Zank et al., 2021). Interplanetary shocks are ubiquitous in the solar wind (e.g. Kilpua et al., 2015), and are  
usually driven by interplanetary coronal mass ejections (ICMEs; e.g., Kilpua et al., 2017) or they are formed ahead of fast–  
35 slow stream interaction regions (e.g., Richardson, 2018; Jian et al., 2006). Several statistical analyses have been conducted to  
investigated how shock waves affect fluctuation power levels and spectral slopes (e.g., Park et al., 2023; Borovsky, 2020; Pitňa  
et al., 2016; Kilpua et al., 2021; Pitňa et al., 2021), including also theoretical considerations (e.g., Zank et al., 2021). They have  
shown that the fluctuation power (and normalised power calculated with the structure function, to a lesser extent) is enhanced  
from the upstream to downstream, while spectral slopes both in the inertial and ion dissipation ranges are unaffected or steepen  
40 somewhat. The enhancement of fluctuation power is related to the compression at the shock and possible generation of new  
fluctuations downstream of the shock. The steeper spectral slopes downstream could be related to an increase of intermittent  
structures such as current sheets. The steepening of the spectral slope (or its invariance) at the shock transition is in contrast to  
observations at planetary bow shocks, where in some cases  $f^{-1}$  range is found in the downstream suggesting that the turbulence  
spectrum is reset (Hadid et al., 2015; Huang et al., 2017, 2020). Such “fresh injection” in the shock downstream has also been  
45 modelled by means of kinetic simulations of shocks interacting with laminar and turbulent plasma, showing its relevance at  
small scales (Trotta et al., 2023).

Also among the key parameters for characterising turbulence are the normalised cross-helicity ( $\sigma_c$ ), residual energy ( $\sigma_r$ )  
and magnetic helicity ( $\sigma_m$ ) (e.g., Matthaeus and Goldstein, 1982; Roberts et al., 1987). The normalised cross-helicity and  
residual energy describe, respectively, how the balance in power between fluctuations propagating parallel and anti-parallel to  
50 the mean magnetic field, and how energy is divided between kinetic (i.e., velocity) and magnetic fluctuations (Bavassano et al.,  
1998; Verscharen et al., 2019; Bruno and Carbone, 2013). These parameters may thus be used to describe ‘Alfvénicity’ in the  
solar wind and they also affect the energisation of charged particles at interplanetary shock waves (Vainio and Schlickeiser,  
1998) by affecting particle scattering close to the shock: If turbulence is Alfvénic, normalised cross-helicity will (1) determine  
the effective scattering centre speed relative to the medium and, thus, the so-called scattering centre compression ratio at the  
55 shock, which governs first-order Fermi acceleration at the shock, and (2) the rate of second-order Fermi acceleration, which  
does not operate in a unidirectional Alfvén wave field. The normalised magnetic helicity (Matthaeus and Goldstein, 1982) in  
turn is defined as the ratio of the magnetic helicity and total energy spectra. Its value is zero for linearly polarised Alfvén wave  
turbulence at MHD scales (in contrast to the kinetic range). It has been shown, both in the interplanetary case (Ruohotie et al.,

2022) and at Earth's bow shock (Trotta et al., 2022), that flux ropes transmitted across shocks increase their magnetic helicity content, with important consequences on a series of key phenomena like particle acceleration (Kilpua et al., 2023).

The imbalance of inertial range cross-helicity and equipartitioning of residual energy increases with heliospheric distance from the Sun (e.g., Bruno and Carbone, 2013; Chen et al., 2020; Tu and Marsch, 1995), i.e., fluctuations propagate increasingly parallel or anti-parallel to the mean magnetic field ( $\sigma_c \sim \pm 1$ ) and power in magnetic and kinetic energies is more equally divided. At the orbit of the Earth residual energy is on average negative (e.g., Perri and Balogh, 2010; Good et al., 2023; Soljento et al., 2023; Chen et al., 2013), and it becomes increasingly negative closer to the Sun (e.g., Chen et al., 2020), meaning that the magnetic energy of fluctuations exceeds the kinetic energy.

Borovsky's (2020) statistical study of inertial range fluctuations associated with 109 shocks with density compression ratio larger than  $\sim 2$  included examination of Alfvénicity as defined in terms of the degree and sign of correlation between the magnetic field and velocity fluctuations and Alfvén ratio. The authors found that Alfvénicity on average decreased at the shock transition from upstream to downstream (region durations 60–120 minutes) regardless of the driver of the shock. Soljento et al. (2023) analysed differences in the distributions of normalised cross-helicity and residual energy upstream and downstream of 74 ICME-driven shock waves, with their study considering the whole sheath region (up to  $\sim 1$  day in duration) downstream of the shock. They found that turbulence became more balanced (i.e. more  $\sigma_c \sim 0$  values) downstream and that there was slightly more energy in magnetic field than in velocity fluctuations (i.e. more negative  $\sigma_r$  values) in the sheath. The latter finding is consistent with the Borovsky (2020) work. These findings are also consistent with the study by Good et al. (2022), who performed a superposed epoch analysis of cross-helicity and residual energy in 176 ICME-driven sheath regions, of which 97 were bounded by shocks. Previous theoretical studies (e.g., Vainio and Schlickeiser, 1998, 1999) and simulations (e.g., Sishtla et al., 2023) may explain the transition from imbalanced to balanced turbulence via the presence of both transmitted (propagating anti-sunward) and reflected (propagating sunward) fluctuations as imbalanced upstream waves interact with the shock.

Most studies on the effect of shocks on normalised cross-helicity, residual energy and magnetic helicity have however been case studies. We summarize in the following some of their key findings. Zhao et al. (2021) analysed an ICME-driven shock wave that was observed on 19 April 2020 by *Solar Orbiter* at 0.8 au and the next day by *Wind* at  $\sim 1$  au. They found that at *Wind* the cross-helicity at the injection scales (time scales from 1 hour upward) was almost zero downstream of the shock, suggesting balanced turbulence with waves propagating both parallel and anti-parallel to the magnetic field. The residual energy in turn changed at the shock transition at *Wind* to a more negative value, indicating more power being in the magnetic field fluctuations. These results are consistent with the statistical studies by Borovsky (2020) and Soljento et al. (2023) covering inertial range fluctuations. Zhao et al. (2021) also noted that inertial range magnetic helicity values, analysed both at *Solar Orbiter* and *Wind*, were enhanced both upstream and downstream of the shock and coincided with increased wave activity. Their observations suggested the presence of kinetic Alfvén waves at the proton cyclotron frequency downstream and lower-frequency and non-compressive ULF range waves excited by streaming particles upstream. Trotta et al. (2024b) studied a strong shock wave that was detected by Parker Solar Probe at 0.07 au on 5 September 2022 and by *Solar Orbiter* at 0.7 au the following day. Similar to Zhao et al. (2021), this event showed enhancement of magnetic helicity close to the proton cyclotron



frequency in the downstream, while the signature disappeared downstream. Using a coupled turbulence transport model and  
95 the *Wind* spacecraft at 1 au, Adhikari et al. (2016) found that the turbulence became more balanced only for parallel shocks  
while for perpendicular shocks  $|\sigma_c|$  values increased. The residual energy instead increased at the shock both for parallel and  
perpendicular shocks.

In this work, we perform to our knowledge the first comprehensive statistical analysis of how the normalised cross-helicity,  
residual energy and magnetic helicity vary at interplanetary shock waves taking into account the effect of the shock properties.  
100 Our analysis uses 371 shocks observed by the *Wind* spacecraft in the near-Earth solar wind and seven shocks observed by *Solar  
Orbiter* between 0.3–0.5 au.

## 2 Data and approaches

### 2.1 Data and event selection

We have used data from the *Wind* (Ogilvie and Desch, 1997) and *Solar Orbiter* (Müller et al., 2020) spacecraft. The *Wind* data  
105 extends from 1995 – 2023, a time range spanning 2.5 solar cycles, while *Solar Orbiter* shocks are analysed for the period 2020  
– 2023, covering the rising phase of Solar Cycle 25.

The magnetic field observations from *Wind* are provided by the Magnetic Fields Investigation (MFI; Lepping et al., 1995)  
and the plasma data by the Three-Dimensional Plasma and Energetic Particle Investigation (3DP; Lin et al., 1995). The nominal  
cadence of the field and plasma data used was 3 s. As the cadence varied slightly, the data were averaged to 10 s cadence.

110 From *Solar Orbiter*, we have used magnetic field measurements from the magnetometer (MAG; Horbury et al., 2020) and  
plasma data from the Solar Wind Analyser (SWA; Owen et al., 2020) suite. Both *Wind* and *Solar Orbiter* data were obtained  
from the NASA Goddard Space Flight Center Coordinated Data Analysis Web<sup>1</sup> (CDAWeb). *Solar Orbiter* was launched on 10  
February 2020. The spacecraft has a heliocentric orbit with a perihelion distance of 0.28 au and aphelion distance of ~1 au. For  
*Solar Orbiter* the nominal cadence of the plasma data was 4 s and for the magnetic field 0.125 s, which were also interpolated  
115 to 10 s cadence.

The shocks were gathered from the Heliospheric Shock database<sup>2</sup> developed and maintained at the University of Helsinki  
(Kilpua et al., 2015) as well as from the Harvard-Smithsonian Center for Astrophysics interplanetary shock database for the  
*Wind* spacecraft<sup>3</sup>. Only fast forward shocks have been analysed in this study. We excluded shocks that had data gaps in the  
upstream or downstream. The *Solar Orbiter* shocks were obtained from the SERPENTINE project shock catalogue<sup>4</sup> (Trotta  
120 et al., 2024a). We selected only those shocks from *Solar Orbiter* that were observed below 0.5 au and for which there were  
both plasma and magnetic field data available without data gaps in their upstream and downstream.

The final set of analysed events includes 371 *Wind* shocks and seven *Solar Orbiter* shocks.

<sup>1</sup><http://cdaweb.gsfc.nasa.gov/>

<sup>2</sup><http://ipshocks.helsinki.fi/>

<sup>3</sup>[https://cfa.harvard.edu/shocks/wi\\_data/](https://cfa.harvard.edu/shocks/wi_data/)

<sup>4</sup><https://data.serpentine-h2020.eu/catalogs/shock-sc25>





## 2.2 Calculation of shock parameters

We divide the analysed shocks into different categories according to their properties that include: the gas compression ratio ( $r_g$ ), i.e. the downstream to upstream density ratio; the upstream plasma beta ( $\beta_u$ ), i.e., the ratio of plasma to magnetic pressure; the velocity jump across the shock ( $\Delta V$ ); and the shock obliquity ( $\theta_{Bn}$ ), i.e., the angle between the upstream magnetic field direction and shock normal. The shock angle  $\theta_{Bn}$  plays a fundamental role in shaping the shock structure and in accelerating charged particles as it controls the dynamics of charged particles close to the shock. Quasi-parallel shocks (Burgess et al., 2005), which have  $\theta_{Bn} < 45^\circ$ , have extended foreshock regions where particles can escape upstream from the shock and, therefore, are related to smaller and more gradual increases in the field magnitude and plasma parameters than quasi-perpendicular shocks (Bale et al., 2005); quasi-perpendicular shocks, which have  $\theta_{Bn} > 45^\circ$ , have particles that stay close to the shock and a sharper shock transition. Other important parameters for shock properties including the generation of upstream fluctuations are the plasma beta and Mach numbers. The upstream plasma beta can affect the shock vicinity by controlling the generation and growth of plasma waves; for example, high plasma beta gives rise to whistler waves and enhances the amplitude of turbulent fluctuations.

The shock parameters for all shocks have been determined using a publicly available software package, SerPyShocks (Trotta et al., 2022), which allows calculation of basic shock properties as a function of mean values calculated over varying upstream and downstream windows. We have used maximum 20-min and minimum 2-min averaging windows for both the upstream and downstream, excluding 1 min before and after the shock. To calculate the speed jumps, only the values obtained using the maximum averaging window (20 min) both for the upstream and downstream have been used.

Shock angles have been estimated using the mixed-mode method, which incorporates both the magnetic field and velocity data in the calculation of the shock normal (Abraham-Shrauner and Yun, 1976; Trotta et al., 2022):

$$\hat{\mathbf{n}}_{sh} = \pm \frac{(\Delta \mathbf{B} \times \Delta \mathbf{V}) \times \Delta \mathbf{V}}{|(\Delta \mathbf{B} \times \Delta \mathbf{V}) \times \Delta \mathbf{V}|}$$

where  $\Delta \mathbf{B}$  and  $\Delta \mathbf{V}$  are changes in the magnetic field and velocity vectors from downstream to upstream, respectively.

## 2.3 Calculation of turbulence parameters

The cross-helicity ( $\sigma_c$ ) and residual energy ( $\sigma_r$ ) can be calculated from the power spectral densities (PSDs) of the velocity and magnetic field. Here the Elsässer variables help to simplify the analysis. These variables were first defined and used by Elsässer (1950) to transform the incompressible magnetohydrodynamic (MHD) equations into a symmetric form. The Elsässer variables are given by  $\mathbf{z}^\pm = \mathbf{v} \pm \mathbf{b}$ , where  $\mathbf{v}$  represents the velocity and  $\mathbf{b} = \mathbf{B}/\sqrt{\mu_0 \rho}$  is the magnetic field in velocity units, where  $\rho$  is the ion density. Fluctuations in  $\mathbf{z}^-$  represent Alfvénic wave packets propagating parallel to the magnetic field, and fluctuations in  $\mathbf{z}^+$  are wave packets propagating anti-parallel to the magnetic field.

As stated in Section 1, the residual energy is defined as the partition of energy between kinetic and magnetic fluctuations, i.e., the difference in the PSD of  $v$  and  $b$ , denoted as  $E_v$  and  $E_b$ , respectively. The quantity is typically normalised to take



values between  $[-1, 1]$ , and is thus calculated as

$$\sigma_r = \frac{E_v - E_b}{E_v + E_b}, \quad (1)$$

with negative (positive) values indicating an excess of magnetic (kinetic) fluctuation power and  $\sigma_r \sim 0$  an equipartition of energy, which is a property of ideal Alfvén waves.

155 The cross-helicity may be defined as the balance between the fluctuations propagating parallel and anti-parallel to the magnetic field, and thus is given by the difference in the PSD of  $\mathbf{z}^+$  and  $\mathbf{z}^-$ . Similar to residual energy, the cross-helicity is also normalised to take values between  $[-1, 1]$ :

$$\sigma_c = \frac{E_+ - E_-}{E_+ + E_-}. \quad (2)$$

160 Here negative (positive) values indicate greater power in fluctuations propagating parallel (anti-parallel) to the background field, and  $\sigma_c \sim 0$  gives the balanced case.

The normalised magnetic helicity (Matthaeus and Goldstein, 1982; Zhao et al., 2021) is calculated as

$$\sigma_m = \frac{2 \operatorname{Im} [W_j^*(\nu, t) \cdot W_k(\nu, t)]}{|W_i(\nu, t)|^2 + |W_j(\nu, t)|^2 + |W_k(\nu, t)|^2}, \quad (3)$$

165 where  $W_i(\nu, t)$ ,  $W_j(\nu, t)$ , and  $W_k(\nu, t)$  are the wavelet transforms of the Cartesian magnetic field components  $i$ ,  $j$  and  $k$  (e.g., the GSE or RTN coordinate systems) and  $\nu$  is the frequency of the wavelet function. The negative values of magnetic helicity indicated left-handed polarised waves while positive values indicate right-handed polarised waves. In the solar wind at  $\sim 1$  au, normalised magnetic helicity in the injection range is on average strongly negative, on average zero in the inertial range and positive in the dissipation range (e.g., Smith, 2003).

170 We have calculated  $\sigma_c$ ,  $\sigma_r$  and  $\sigma_m$  in 1-hr regions both upstream and downstream of the shocks, excluding 1-min intervals immediately before and after the shock time. The wavelet spectrograms were calculated separately for these intervals, and values outside the cone-of-influence have been removed. Probability distribution functions (PDFs) have been built for  $\sigma_c$ ,  $\sigma_r$  and  $\sigma_m$  for all shocks, as well as for shock subsets separated by the shock parameters.

175 The direction of the interplanetary magnetic field (IMF), which defines the IMF sector, can be either towards or away from the Sun. Thus whether fluctuations in  $\mathbf{z}^\pm$  correspond to sunward or anti-sunward fluctuations is dependent on the IMF sector. To explore in more detail how the shock transition affects the relative power in sunward and anti-sunward propagating waves, we also find the rectified cross-helicity,  $\sigma_c^*$ , where  $\mathbf{z}^+$  ( $\mathbf{z}^-$ ) fluctuations are fixed to always corresponds to anti-sunward (sunward) fluctuations, and positive (negative)  $\sigma_c^*$  indicates an anti-sunward (sunward) imbalance. For data in GSE coordinates, the *towards* sector is defined as having an IMF clock angle  $\phi$  below  $45^\circ$  or over  $225^\circ$ , while in the *away* sector  $\phi$  is in the interval  $[45^\circ, 225^\circ]$ ; the Parker spiral  $\phi$  angles are, thus,  $315^\circ$  and  $135^\circ$  in the towards and away sectors, respectively. To perform the rectification, the magnetic field sign is flipped when the IMF is in the away sector before calculating the cross-helicity. For 180 this analysis, we only use cases where the IMF stays consistently in one sector throughout the 2 hr interval investigated to avoid inconsistencies from IMF sector reversals. This part of the analysis was only performed for the *Wind* shocks due to the relatively low number of *Solar Orbiter* shocks available. In total, 233 *Wind* shocks were investigated for their effects on  $\sigma_c^*$ .



### 3 Results

#### 3.1 Example events

185 Here we describe a few examples from the full set of analysed events.

Figure 1 shows a shock detected at *Wind* on 8 July 2019 at 18:26 UT. The shock was nearly perpendicular, with  $\theta_{Bn} = 83.9^\circ$ , moderate values of  $\Delta V = 45.5 \text{ km s}^{-1}$  and  $r_g = 2.0$ , and  $\beta_u = 2.1$ . The IMF cone angle was consistently in the towards sector during the 2-hr period shown and thus positive  $\sigma_c$  values (red) indicate anti-sunward propagation and negative  $\sigma_c$  values (blue) sunward propagation. The upstream region was dominated by anti-sunward fluctuations at all frequencies, but there were some  
190 local patches of predominantly sunward fluctuations and fluctuations with  $|\sigma_c| \sim 0$ . The turbulence in the upstream is however globally balanced (Chen et al., 2013), indicated by the average value of  $|\sigma_c|$  being 0.20. The fluctuations in the downstream region are also relatively balanced with the average  $|\sigma_c| = 0.28$  but now, in contrast to the upstream, sunward fluctuations dominate. The residual energy was mostly negative in the upstream with the average value of  $\langle \sigma_r \rangle = -0.48$ , indicating a clear excess of magnetic fluctuation energy, while in the downstream the average is  $\langle \sigma_r \rangle = -0.19$  showing global equipartitioning.  
195 The downstream region closest to the shock exhibits patches with more power in kinetic fluctuations whereas the region deeper in the downstream is dominated by patches with more power in magnetic fluctuations. The magnetic helicity in turn did not show clear changes from the upstream to downstream, having values mostly quite close to zero as is usually the case in the inertial range for solar wind at 1 au (see Section 2.3). The average magnetic helicities in the upstream and downstream are  $-0.024$  and  $-0.073$ , respectively.

200 Another example of a shock detected by *Wind* is shown in Figure 2, which occurred on 31 October 2001 at 13:47 UT. It was nearly parallel, with  $\theta_{Bn} = 9.69^\circ$ ,  $\Delta V = 68.7 \text{ km s}^{-1}$ ,  $r_g = 3.3$ , and  $\beta_u = 1.4$ . The IMF was in the away sector and so anti-sunward fluctuations had negative (blue) and sunward fluctuations positive (red) cross-helicity values. The majority of fluctuation power in both the upstream and downstream was anti-sunward. The upstream is clearly unbalanced with average  $|\sigma_c| = 0.64$  while in the downstream cross-helicity is again relatively balanced with average  $|\sigma_c| = 0.30$ . The residual energy  
205 showed significant equipartition in the upstream region (average  $\sigma_r = -0.027$ ) with patches of negative and positive values. The downstream region was instead characterised by dominantly negative residual energy ( $\sigma_r = -0.27$ ), except for a localised region just after the shock. Both the upstream and downstream regions had significant instances of strong magnetic helicity at all frequencies, particularly in the upstream. The average  $\sigma_m$  values were however again close to zero with values  $-0.059$  and  $-0.036$  in the upstream and downstream, respectively.

210 The cyan and pink contours in the bottom panels of Figures 1 and 2 delineate regions fulfilling the criteria for Alfvén waves and small-scale flux ropes; this aspect of the analysis is discussed in Section 3.3.1.

#### 3.2 Shock parameters

Figure 3 shows histograms of the selected shock parameters, namely the gas compression ratio (i.e. downstream-to-upstream density ratio), plasma beta, velocity jump and shock angle across all 371 shocks from the *Wind* spacecraft, and also for the  
215 233 shocks for which the rectified cross-helicity ( $\sigma_c^*$ ; Section 2.3) could be determined. The solid vertical lines indicate the



medians and the dashed lines give the 20th and 80th percentiles that we later use to divide the shocks into two subsets. These percentiles were chosen to give sufficiently distinct populations but with a sufficiently large number of events (74 in each of the subsets) for the robust statistical analysis.

220 The median values of  $r_g$  are slightly over 2.0 for all events and for those used in the  $\sigma_c^*$  analysis. The histograms are biased towards small  $r_g$  values but have tails that extend to  $r_g > 4$ , i.e., beyond the theoretical limit for perpendicular MHD shocks. For the majority of shocks,  $\beta_u > 1$ , with the distributions having long  $\beta_u$  tails. The 20th percentile of  $\beta_u$ , however, is at 0.89; the 20th percentile subset thus represents cases where the magnetic pressure dominates in the upstream. The upper quartile population with  $\beta_u \gtrsim 3$  represent in turn cases that have their upstream beta clearly above the typical solar wind values, ( $\beta_u \sim 1 - 2$ ; e.g., De Keyser et al., 2001; Mullan and Smith, 2006).

225 The  $\Delta V$  distribution peaks at  $\sim 70 \text{ km s}^{-1}$  with a tail extending to  $\Delta V \sim 250 \text{ km s}^{-1}$ . Finally, the  $\theta_{Bn}$  angles indicate a clear preponderance of quasi-perpendicular shocks ( $\theta_{Bn} > 45^\circ$ ) with the median being  $61^\circ$ . As discussed in Kilpua et al. (2015), this could be partly a selection bias as quasi-parallel shocks are more difficult to identify from the ambient wind due to their tendency for more gradual transitions from upstream to downstream, complex structure of the shock surroundings, and more modest field jumps. However, the shocks in the 20th percentile subset are all in the quasi-parallel regime ( $\theta_{Bn} < 45^\circ$ ).

### 230 3.3 Statistical results at 1 au

#### 3.3.1 Shock influence on turbulence parameters

We first investigate how the turbulence parameters in the upstream and downstream depend on the selected shock parameters. The results are shown in Figure 4 for the individual events in the upstream (darker colours) and downstream (lighter colours). The values are calculated from the wavelet spectrograms over frequencies 1.67-16.7 mHz (1-10 min timescales), which fall 235 within the inertial range of MHD turbulence (e.g., Bruno and Carbone, 2013; Verscharen et al., 2019) at the orbit of the Earth. The curves in Figure 4 give 40-event running medians.

The points in the two top panels show the absolute values of the 1-hr averages of normalised cross helicity ( $|\langle \sigma_c \rangle|$ ) and 1-hour averages of the rectified cross helicity ( $\langle \sigma_c^* \rangle$ ). We have chosen to show the absolute values of the averages for the cross-helicity to give a better estimate of how balanced or imbalanced the turbulence is. This is because the balance and imbalance 240 are global rather than local properties (e.g., Chen et al., 2013), and taking the magnitude first would lose information about the global signed average. As detailed in Section 2.3, the rectified cross-helicity fixes the propagation direction with respect to the Sun; negative rectified cross helicity indicates sunward propagation and positive values represent anti-sunward propagation in the plasma frame. The two bottom panels show the averages of the residual energy and magnetic helicity ( $\langle \sigma_r \rangle$  and  $\langle \sigma_m \rangle$ , respectively).

245 Before discussing the dependence on the shock characteristics, we will summarise some overall properties of the investigated turbulence parameters. Firstly, the two top panels of Figure 4 show that  $|\langle \sigma_c \rangle|$  and  $\langle \sigma_c^* \rangle$  spread over all possible values. The means over the whole data set are shown in Table 1 as well as the percentage of the events that had  $|\langle \sigma_c \rangle| < 0.3$ , i.e. globally balanced fluctuations and  $|\langle \sigma_c \rangle| > 0.5$ , i.e. globally imbalanced fluctuations. Both in the upstream and downstream about one-



third of the events have balanced fluctuations while the upstream has considerably more imbalanced events, 50% compared  
 250 to 40%, respectively. The fluctuations propagate dominantly anti-sunward as featured by the clear majority of  $\langle\sigma_c^*\rangle$  values  
 being positive (over 80%, Table 1). The residual energies are in turn nearly all negative indicating that magnetic energy in  
 fluctuations dominates over kinetic energy. According to Table 1 the percentage of the events where fluctuations are close  
 to global equipartition, i.e.,  $|\langle\sigma_r\rangle| < 0.3$ , is considerably higher for the upstream than for the downstream (46% and 36%,  
 respectively). Finally, Figure 4 shows that the average magnetic helicities are clustered around zero.

**Table 1.** The first four rows give the means of the 1-hour averaged turbulence parameters in the upstream and downstream. The next rows give  
 the percentages of the events for which fluctuations are balanced, imbalanced, propagate dominantly antisunward and close to equipartition.  
 The last two rows give the mean percentage occurrence of periods fulfilling Alfvén wave (AF) and flux rope (FR) criteria (Section 3.3.3).

	upstream	downstream
mean $ \langle\sigma_c\rangle $	0.49	0.43
mean $\langle\sigma_c^*\rangle$	0.38	0.36
mean $\langle\sigma_r\rangle$	-0.33	-0.35
mean $\langle\sigma_m\rangle$	$\sim 0$	$\sim 0$
balanced ( $ \langle\sigma_c\rangle  < 0.3$ )	31%	32%
imbalanced ( $ \langle\sigma_c\rangle  > 0.5$ )	50%	40%
anti-sunward ( $\langle\sigma_c^*\rangle > 0$ )	82%	84%
equipartitioned ( $ \langle\sigma_r\rangle  < 0.3$ )	46%	36%
mean AF occurrence	14.8%	10.8 %
mean small FR occurrence	1.1%	1.7 %

255 Figure 4 shows a large scatter as a function of the displayed shocks parameters for all cases but some trends are visible. The  
 $|\langle\sigma_c\rangle|$  values (also the rectified ones) are the highest, i.e., feature the highest imbalance, for  $r_g \sim 2.5$  after which the median  
 curves clearly decline towards more balanced fluctuations. This decline after the peak  $|\langle\sigma_c\rangle|$  has been reached is stronger  
 for the downstream. The second columns in the top rows show that the cross-helicities both in the upstream and downstream  
 exhibit the highest imbalance of fluctuations for  $\beta_u \sim 1 - 2$ , which are, as previously mentioned, common 1 au values. For  
 260 the lowest ( $\beta_u \lesssim 1$ ) and higher ( $\beta_u \gtrsim 3$ ) upstream beta values a considerably smaller fraction of fluctuations are imbalanced  
 (except for the very largest plasma beta, but the number of events too small to draw strong conclusions). Both the upstream and  
 downstream also exhibit clear increase of  $|\langle\sigma_c\rangle|$  and  $\langle\sigma_c^*\rangle$  with the increasing shock velocity jump up to  $\Delta V \sim 100 - 150 \text{ km s}^{-1}$   
 after which in the upstream the curves level off while in the downstream fluctuations become again more balanced. Finally,  
 the last panel in the top row shows that there is a weak tendency for fluctuations to be more balanced for quasi-perpendicular  
 265 shocks than for quasi-parallel shocks, but the median curves show large fluctuations and there are relatively few parallel shocks  
 in the distribution.

The  $\langle\sigma_r\rangle$  and  $\langle\sigma_m\rangle$  do not show such obvious trends with the shock parameters as was previously found for the cross-  
 helicities. The residual energy values exhibit a weak trend towards zero (fluctuations becoming more equipartitioned) with



increasing  $\Delta V$  and towards increasingly negative values with the increasing shock angle. In addition, similar to the most  
270 imbalanced fluctuations, the highest equipartitioning occurs for the upstream plasma beta in the range  $\sim 1 - 2$ .

### 3.3.2 Change of turbulence parameters at the shock

We will investigate next how the average values of normalised residual energy, cross-helicity and magnetic helicity change  
across the shock as a function of the shock properties. The heatmaps in Figure 5 show relative occurrences in bins defined by  
the values of the shock parameters and change from the upstream to downstream (i.e., the upstream value subtracted from the  
275 downstream value) of  $\langle |\sigma_c| \rangle$ ,  $\langle |\sigma_r| \rangle$ , and  $\langle |\sigma_m| \rangle$ . Relative occurrences have been calculated by dividing the number of events  
in a given bin with the total number of events in the corresponding shock parameter range. This approach was chosen as the  
number of events varies considerably with the shock parameters, as shown in Figures 3 and 4. The white solid curves give the  
40-event running medians of the percentage differences and the dashed curves the upper and lower quartiles.

In the top row, positive (negative) percentages mean that the upstream (downstream) had more balanced  $\sigma_c$  and in the  
280 middle row that the upstream (downstream) kinetic and magnetic energies were closer to equipartition. In the bottom panels,  
large positive (negative) values indicate that the downstream (upstream) has potentially more coherent structures, either Alfvén  
waves or small-scale flux ropes. Since the  $\beta_u$  had a long tail to high values with only a few events we have limited the range in  
the plot for clarity.

Firstly, Figure 5 shows that the upstream to downstream change in  $\langle |\sigma_r| \rangle$  and  $\langle |\sigma_m| \rangle$  values between upstream and down-  
285 stream are generally much smaller than for  $\langle |\sigma_c| \rangle$  (note different y-scales in top row and other two rows).

The top row of Figure 5 shows that for the individual events the fluctuations in the downstream are typically more balanced  
compared to the upstream (i.e., the change from the upstream to downstream is negative). However, there is a considerable  
fraction of events for which the upstream is more balanced than the downstream (39% from total 371 events). The tendency for  
the downstream to be more balanced than the upstream increases with the increasing shock gas compression ratio and shock  
290 velocity jump. In particular, for  $r_g \gtrsim 2.5$  and  $\Delta V \gtrsim 150 \text{ km s}^{-1}$  the change is negative for the majority of the cases. We also note  
that in our example events in Section 3.1 the first case with smaller  $r_g$  had more balanced upstream while the second event with  
larger  $r_g$  had imbalanced upstream and balanced downstream. For the shock angle and upstream plasma beta, no clear trend is  
visible.

The middle panels in Figure 5 show that the upstream to downstream change in  $\langle |\sigma_r| \rangle$  is slightly more frequently positive  
295 than negative signifying that kinetic and magnetic energies of fluctuations tend to be in closer equipartition in the upstream  
than in the downstream. This is particularly true for shocks associated with large velocity jumps ( $\gtrsim 150 \text{ km s}^{-1}$ ). For  $\langle |\sigma_m| \rangle$   
in turn the only notable (weak) trend is that the values tend to be negative for quasi-parallel shocks which could indicate the  
more frequent presence of high magnetic helicity structures in the upstream compared to downstream. We examine this in more  
detail in Section 3.3.3.

300 To further explore changes related to the shock properties, we present in Figures 6 and 7 how the probability density functions  
(PDFs) of  $\sigma_c$ ,  $\sigma_r$  and  $\sigma_m$  vary from the upstream to downstream. The PDFs combine all values from the wavelet spectrograms





in the 16.7 mHz -16.7 mHz frequency range (1 to 10 minutes time scale range) in shock subgroups based on the 20th and 80th percentiles of the selected shock parameters (see Figure 3).

We first note that the PDFs for magnetic helicity  $\sigma_m$  are nearly symmetric around  $\sigma_m = 0$ , consistent with previous studies  
305 finding that the magnetic helicity averages to zero in the inertial range in the solar wind. Secondly, their PDFs show very little difference between the upstream and downstream for all investigated cases. Therefore, in the following, we discuss only variation in the PDFs for the cross-helicity and residual energy.

The top two rows in Figure 6 show how the PDFs change depending on the shock gas compression ratio. The top rows give the PDFs for the subset with gas compression ratios within the 80th percentile ( $r_g > 2.8$ , and for  $\sigma_c^* r_g > 2.69$ ) while the next  
310 row gives the PDFs for compression ratios within the 20th percentile ( $r_g < 1.72$ , and for  $\sigma_c^* r_g > 1.67$ ). The cross helicity PDFs are almost identical upstream and downstream for the shocks with small  $r_g$ , while for the 80th percentile subgroup significant changes occur, as follows: In agreement with Figure 5, the cross-helicity PDFs show that fluctuations on average are clearly more balanced downstream than in the upstream at large  $r_g$ , with a strong decrease in  $\sigma_c \sim \pm 1$  values and enhancement in values between  $\sigma_c = -0.5$  and  $0.5$ . The rectified cross helicity ( $\sigma_c^*$ ) reveals that both in the upstream and downstream the  
315 waves propagate dominantly anti-sunward. It also reveals that for the upper quartile population, both the sunward ( $\sigma_c^* \sim -1$ ) and anti-sunward ( $\sigma_c^* \sim +1$ ) cross-helicities decrease from upstream to downstream, with a stronger decrease observed for the anti-sunward waves. The enhancement from upstream to downstream occurs around  $\sigma_c^* \sim 0$ , indicating that fluctuations become more balanced.

The peak of the residual energy PDF for the  $r_g$  upper quartile population in turn shifts to considerably more negative values  
320 and becomes slightly flatter from upstream to downstream, indicating that fluctuations in the downstream have increasingly more power in magnetic than kinetic fluctuations. For the lower quartile population in turn, the differences between the upstream and downstream PDFs are minimal.

The two bottom rows of Figure 6 show the PDFs for the 80th and 20th upstream plasma beta percentiles. The plasma beta has relatively little effect on how the combined PDFs change at the shock. There are, however, some interesting differences  
325 between the PDFs for the high and low beta cases that were not so evident from the previously shown averaged values. Firstly, the cross-helicities are considerably more balanced for high  $\beta_u$  shocks than for low  $\beta_u$  shocks. For high  $\beta_u$  shocks the rectified cross-helicity PDFs peak at  $\sigma_c^* \sim 0$  while for low  $\beta_u$  the anti-sunward waves clearly dominate the distribution. In addition, the residual energy PDFs for low  $\beta_u$  shocks peak close to zero (indicating equipartition in magnetic and kinetic power), while for high  $\beta_u$  shocks the distribution is biased at negative values.

The top two rows in Figure 7 show PDFs for the 80th and 20th percentile velocity-jump subsets. The shocks with small velocity jumps have almost identical PDFs in the upstream and downstream, but the cross-helicity and residual energy PDFs  
330 again differ considerably for shocks with large  $\Delta V$ : In the upstream, fluctuations are highly imbalanced with strong bias towards waves propagating dominantly anti-sunward ( $\sigma_c^* \sim 1$ ) but there is also a population of sunward waves ( $\sigma_c^* \sim -1$ ) not visible for the other investigated subsets. In the shock transition, the anti-sunward population decreases strongly and turbulence becomes  
335 more balanced downstream. Similar to what was observed to  $r_g$  upper quartile subset, the residual energy PDF flattens and the



peak shifts towards more negative values from upstream to downstream. For shocks with small speed jumps the residual energy values are also peaked towards negative values both upstream and downstream, resembling the downstream PDF for high  $\Delta V$ .

For the shock angle, the differences in PDFs are relatively small between the upstream and downstream, both for the quasi-parallel and quasi-perpendicular shocks. A key difference is that the PDFs show turbulence becoming less imbalanced downstream for quasi-perpendicular shocks. Again, there are some noteworthy differences between the two subsets. The cross-helicities are more imbalanced and residual energies show higher equipartition for parallel shocks than for perpendicular shocks.

### 3.3.3 Alfvénic fluctuations and small flux ropes at the shock

The investigated turbulence parameters provide a mean to identify small-scale flux ropes (SFRs) and Alfvénic fluctuations (AFs) from the solar wind plasma and magnetic field measurements. We adopt the same approach and criteria used by Zhao et al. (2021) and Ruohotie et al. (2022), who investigated SFR and AF occurrence using Parker Solar Probe and *Wind* data.

For SFRs, we require that they exhibit a large magnetic helicity, with  $|\sigma_m| > 0.7$ . For AFs, we require that  $|\sigma_m| > 0.7$  or  $|\sigma_m| > 0.3$  for circular or linearly polarized waves, respectively. By definition, AFs have significant v-B correlations or anti-correlations, and so the criterion  $|\sigma_c| > 0.9$  is imposed. Flux ropes in turn are known to have low cross-helicity (i.e. the absence of the v-B correlations or anti-correlations of AFs) and so  $|\sigma_c| < 0.4$  is required. Idealised Alfvénic fluctuations have equipartition of energy between magnetic and kinetic fluctuations, and  $|\sigma_r| < 0.3$  is thus required for AF identification; in contrast, FRs are magnetically dominated, with a requirement of  $|\sigma_r| < -0.5$  set here for their identification. The identification of AFs and SFRs is made here by imposing the above described criteria on the wavelet spectrograms of  $\sigma_c$ ,  $\sigma_r$ ,  $\sigma_m$  in the frequency band 1.67–16.7 mHz (1 to 10 min) as visualised in figures 1 and 2 with the regions that met all of the criteria are shown as cyan (AFs) and pink (SFRs) contours in the bottom panels.

Figure 8 shows how the 30- (gray) and 60-(black) event running medians of the occurrence percentage of AFs and SFRs in the upstream and downstream depend on the shock characteristics. The occurrence percentages are calculated here as the number of bins in the wavelet spectrograms that meet the AF or FR criteria above divided by the total number of bins. The shaded areas indicate the interquartile range for the 30-event medians.

Firstly, Figure 8 reveals that there considerably more intervals fulfilling the AF criteria than the SFR criteria, and that the shock upstream has more AFs but less SFRs than the downstream (note different y-axis scales in the figure). The mean occurrence percentages of AFs are 14.8% and 10.8%, and for SFRs 1.1% and 1.7% in the upstream and downstream, respectively (Table 1). The occurrence of AFs both in the upstream and downstream peak with  $\beta_u \sim 1 - 2$ , and is lowest for the most perpendicular shocks. There is no obvious trend with the gas compression ratio but for  $r_g \gtrsim 3$ , the occurrence of AFs drops significantly. In the downstream, the AF occurrence clearly increases with increasing  $\Delta V$ , while in the it peaks for  $\Delta V \sim 100 - 150$  km/s, and for quasi-parallel shocks.

The bottom two rows show that the SFR occurrence both in the upstream and downstream increases with increasing  $\beta_u$ . In the upstream there is a weak declining trend in the SFR occurrence with the increasing shock velocity jump while in the downstream the SFRs occurrence increases with increasing  $r_g$ . In contrast to AFs, there is no trend with the shock angle.



370 The heatmaps in Figure 9 show the relative change in the AF and FR percentage occurrences. Similar to Figure 5 relative occurrence rates are calculated by dividing the number of events in a bin with the total number of events in the corresponding shock parameter range. The 40-event running medians with the upper and lower quartiles are also shown.

In agreement to Figure 8, on average, the individual events also feature that the change in the percentage occurrence for AFs from the upstream to downstream is negative, i.e. the upstream has more AFs than the downstream, while more SFRs occur in  
375 the downstream. The opposite changes are however observed in both cases.

The tendency for upstream to have more AFs than the downstream is the largest for shocks associated with  $r_g \gtrsim 2.5$ ,  $\beta_u \lesssim 2$ , and  $\Delta V \gtrsim 100$  km/s. The SFRs are the most abundant in the downstream when compared to the upstream when the upstream beta and velocity jumps are large.

The decrease in the AF occurrence and increase in the FR occurrence across the shock are obvious for our example event  
380 shown in Figure 2. In the upstream region there are several regions that meet the criteria for the AFs (surrounded by cyan contours) for all frequencies while in the downstream AFs have largely disappeared but there are several regions meeting the criteria for FRs (surrounded by pink countours). This was a parallel shock with a large gas compression ratio. The example event in Figure 1 in turn is a case where the bins fulfilling the FR criteria diminish from upstream to downstream. This shock had a similar speed jump but was almost perpendicular.

### 385 3.4 Near-Sun observations

Finally, we investigate whether similar changes in turbulence parameters are observed close to the Sun. Here we analyse seven shocks observed by *Solar Orbiter* below 0.5 au, see Section 2.1. The values of the shock parameters for each shock, including their means and standard deviations, are given in 2. The event-to-event variations in shock parameters are substantial as also indicated by relatively large standard deviations, but compared to *Wind* shocks, the shocks observed by solar orbiter have  
390 on average somewhat higher gas compression ratio and lower upstream plasma beta, while four of them are associated with substantially larger velocity jumps. The shocks are also more parallel, from seven analysed shocks four are in the quasi-parallel regime ( $\theta_{Bn} < 45^\circ$ ).

The combined PDFs of  $\sigma_c$ ,  $\sigma_r$  and  $\sigma_m$  for seven shocks are shown in Figure 10. The results show an overall similar behaviour as at 1 au, i.e., the fluctuations become more balanced and magnetically dominated from upstream to downstream. The residual  
395 energy PDFs resemble most that of the *Wind* upper quartile population while cross-helicity PDF shows less obvious decrease in balance between upstream and downstream.

Figure 11 shows an example event from *Solar Orbiter*. The spacecraft detected a shock on 10 October 2023 22:32 UT when the spacecraft was 0.3 au from the Sun. The shock was just at the threshold between being quasi-parallel and quasi-perpendicular with  $\theta_{Bn} = 43^\circ$ , and the gas compression ratio had a relatively large value of 3.2. The speed jumps from about  
400 390 km/s to almost 800 km/s at the shock. The *Solar Orbiter* data is given in RTN (Radial - Tangential - Normal) coordinates. In the RTN system, the outward (away) polarity is at clock angle  $\phi$  below  $45^\circ$  or over  $225^\circ$ , while in the *toward* sector  $\phi$  is in the interval  $45^\circ - 225^\circ$ .



In the example event, the IMF is consistently in the toward sector. Thus the positive cross-helicity, which indicates waves travelling anti-parallel to the magnetic field, corresponds to the typically observed anti-sunward propagation. The upstream is imbalanced with average  $|\sigma_c| = 0.60$ . In the downstream, there are some negative cross-helicity patches suggesting the presence of sunward propagating waves as well, and fluctuations are less imbalanced with average  $|\sigma_c| = 0.36$ . The residual energy clearly becomes more negative from upstream to downstream, with the average  $\sigma_r$  changing from -0.18 to -0.62. The last panel shows many areas meeting the criteria for Alfvén waves in the upstream, with only a few regions meeting the criteria for the flux ropes. Unlike at 1 au the upstream  $\sigma_m$  does not average to zero, having a value -0.17. While in the downstream it is -0.069. In the downstream, the trend is reversed with considerably more regions meeting the flux rope criteria but average  $\sigma_m$  is now closer to zero (-0.069)

**Table 2.** The shock parameters for seven shocks included from *Solar Orbiter*. The last row gives the mean values with standard deviations shown in parenthesis.

Date & Time [UT]	r [au]	$r_g$	$\beta_u$	$\Delta V$ [°]	$\theta_{Bn}$ [kms <sup>-1</sup> ]
2022-03-08 14:46	0.48	2.32	0.32	59	53.1
2022-03-11 19:52	0.44	2.87	0.29	281	25.6
2022-04-03 04:52	0.36	2.33	0.74	141	42.2
2023-04-10 04:33	0.29	1.83	1.26	125	23.4
2023-09-19 02:23	0.47	2.31	4.11	44	82.1
2023-09-20 00:47	0.46	2.40	1.71	78	54.0
2023-10-10 22:32	0.30	3.17	1.14	376	43.2
Mean (std)		2.46 ± 0.40	1.36 ± 1.22	158 ± 116	46.3 ± 18.4

#### 4 Discussion

Our investigation of 1-hour averaged inertial range values of normalised cross-helicity ( $\sigma_c$ ), residual energy ( $\sigma_r$ ) and magnetic helicity ( $\sigma_m$ ) in the vicinity of interplanetary shocks are in overall agreement with ~1 au solar wind values reported in previous literature (see the introduction); we found that on average, fluctuations are more frequently imbalanced ( $|\langle\sigma_c\rangle| > 0.5$ ) than balanced ( $|\langle\sigma_c\rangle| < 0.3$ ), outward fluctuation energy dominates (rectified cross helicity  $\sigma_c^* \sim 1$ ), magnetic energy of fluctuations clearly exceeds their kinetic energy (negative  $\sigma_r$ ), and magnetic helicity values average to zero. Cross-helicities exhibited a large variability, consistent with previous studies, which have also shown that their values vary with heliospheric distance and latitude, solar cycle phase as well as with solar wind properties and large-scale structures (e.g., Bruno and Carbone, 2013; Soljento et al., 2023; Good et al., 2023; Perri and Balogh, 2010; D’Amicis et al., 2007, 2011; Chen et al., 2020; Bavassano et al., 1998). As our study spans over 2.5 solar cycles, a significant spread in turbulence parameters could be at least partially explained by variations in the solar wind into which the shocks propagate.



However, most interplanetary shocks observed in the ecliptic plane propagate into relatively slow solar wind (e.g. Kilpua et al., 2015). This is the case also for our data set, which has a mean upstream solar wind speed of  $397 \text{ km s}^{-1}$  and standard deviation of  $84.7 \text{ km s}^{-1}$ . Although antisunward imbalance in  $\sigma_c$  is particularly strong in the fast solar wind (e.g., Matthaeus and Goldstein, 1982; Bavassano et al., 1998), it has been detected in the slow solar wind at 1 au (e.g., D'Amicis et al., 2011, 2021). The outward imbalance likely results from anti-sunward propagating Alfvénic fluctuations. As previously mentioned, Alfvén waves (AF) are locally characterised by high  $|\sigma_c|$  and equipartition of  $\sigma_r$ , with an antisunward imbalance typically observed when averaging over longer intervals.

It is well known that shocks in space plasmas (e.g. planetary bow shocks, interplanetary shocks) generate AFs that propagate upstream via instabilities induced by shock-accelerated ions (Lee, 1982). In the case of forward propagating interplanetary shocks, like those analyzed in the present work, an enhanced presence of anti-sunward AFs is thus expected to increase the imbalance of  $\sigma_c$ . Theoretical work indicates that quasi-parallel and strong shocks are most effective in self-generating AFs (Vainio and Spanier, 2005). This is in agreement with our results on how  $\sigma_c$  and  $\sigma_r$  depend on shock parameters with further evidence of this phenomenon provided our investigation of the presence of AFs using criteria imposed on  $\sigma_c$ ,  $\sigma_r$  and  $\sigma_m$ . The occurrence of intervals fulfilling the criteria for AFs was clearly higher both in the upstream and downstream for quasi-parallel than for quasi-perpendicular shocks. While imbalance in  $\sigma_c$  and occurrence of AF-like intervals first increased with increasing gas compression ratio and shock velocity jump, at more extreme values, the fluctuations become again more balanced and less equipartitioned, and the occurrence AF-intervals decreased, particularly in the downstream. This could be due to the strongest shocks generating compressive fluctuations that reduce Alfvénicity. The increase of imbalance with the increasing velocity jump could also result if the high velocity-jump shocks tend to have higher upstream solar wind speeds (and thus higher imbalance). However, the linear Pearson correlation coefficient calculated between the mean shock velocity jump and the upstream solar wind speed for our data set is only 0.33, indicating weak correlation.

Our study also confirms some previous findings related to how turbulence parameters change across the shock, and gives new insight on how their changes depend on the shock parameters. In agreement with previous studies (e.g., Zhao et al., 2021; Borovsky, 2020; Good et al., 2022; Soljento et al., 2023, see the introduction) we found that fluctuations in the shock upstream tend to be in higher equipartitioning and more imbalanced than in the downstream with anti-sunward fluctuations clearly dominating. The increase in balance at the shock transition occurred particularly for shocks with large velocity jump and gas compression ratio. This could result from anti-sunward fluctuations not transmitting to downstream and / or generation of sunward propagating AFs or non-Alfvénic (compressional) fluctuations. We found that outward rectified cross-significantly decreased across the shock, consistent with AFs not passing to downstream, while residual energy becoming less equipartitioned with higher power in magnetic fluctuations suggests that new non-Alfvénic fluctuations may also be created.

We observed, however, a substantial number of events in which fluctuations became more imbalanced and equipartitioned from upstream to downstream. These cases were mostly related to shocks with smaller gas compression ratio and velocity jumps, in agreement with the assumption that such shocks do not generate AFs effectively. One scenario in which imbalance could increase across the shock is where AFs generated by the shock in the upstream propagate more slowly than the shock, causing them to be left behind and subsequently overtaken by the shock, thus eventually becoming downstream waves.



The PDFs of residual energy and rectified cross-helicity in this study are in general agreement with those reported in Soljento et al. (2023) who compared them between the upstream wind, sheath and ejecta associated with 70 shocks detected by the *Wind* spacecraft. The authors found that  $\sigma_c^*$  values were clearly more balanced in the sheath than in the preceding solar wind, while the differences in  $\sigma_r$  PDFs between different regions were relatively small. This could be because they did not separate the events according to the shock parameters and considered the whole sheath instead of the 1-hour intervals upstream and downstream.

Our identification of more small flux ropes (SFRs) in the shock downstream and more AFs in the upstream is also consistent with a statistical study by Ruohotie et al. (2022) that covers CME-driven sheath regions, with their high frequency range (1-10 mHz) corresponding roughly to the range in our study. As discussed above, periods fulfilling the AF criteria were the most abundant in the upstream compared to downstream for shocks with large velocity jumps, gas compression ratios and quasi-parallel shock configurations, in agreement with theories of shock self-generation of AFs. The observed trend that the occurrence of AFs peaks strongly (both upstream and downstream) with  $\beta_u \sim 1 - 2$ , and that the occurrence of SFRs in the downstream increases with increasing  $\beta_u$  are interesting. The trend for AFs could be explained by their damping in high-beta plasma (e.g., Völk and Cesarsky, 1982; Hollweg, 1971; Squire et al., 2017). SFRs can result from magnetic reconnection and be self-generated from the turbulence cascade (e.g., Zheng and Hu, 2018). In addition, the passage of interplanetary shock past current sheets in the solar wind may trigger reconnection in them and breakdown to magnetic islands / flux ropes (e.g., Odstreil and Karlicky, 1997; Nakanotani et al., 2021). This could explain the the observed trend between  $\beta_u$  and the SFR occurrence, as well as why for high  $\beta_u$  shocks the occurrence of SFRs increases from upstream to downstream. In addition, higher intermittency and steeper spectral indices found in the CME-driven sheaths than in their upstream (Kilpua et al., 2021), support that current sheets could be generated in the shock downstream. Furthermore, reconnecting structures are frequently observed downstream of the Earth's bow shock both in simulations and observations without strong dependence on shock orientation or Mach number (e.g., Gingell et al., 2020, 2023).

The studies looking heliospheric evolution of global values  $\sigma_c$  and  $\sigma_r$  have found that inertial range fluctuations become more balanced and more equipartitioned with increasing distance from the Sun (e.g., Chen et al., 2020). The seven *Solar Orbiter* shocks detected below 0.5 au showed qualitatively similar behaviour as 1 au shocks, featuring also decrease in AWs and increase of SFRs from upstream to downstream.

## 5 Conclusions

We have performed a statistical analysis of the inertial scale normalised cross-helicity, residual energy and magnetic helicity upstream and downstream of 371 interplanetary shocks waves detected by the *Wind* spacecraft at 1 au and 7 shocks detected by *Solar Orbiter* < 0.5 au. We found that in the shock vicinity average residual energies are negative (magnetic energy dominates), magnetic helicities average to zero and cross-helicities have a large spread with preference for antisunward imbalance, in agreement with general solar wind observations. Our study shows that shock transition may significantly affect the investigated turbulence parameters. While weak shocks do not typically significantly alter turbulent properties, shocks with large gas com-





pression ratio and velocity jumps have a clear effect; fluctuations become more balanced and less equipartitioned downstream, implying to the generation of new compressive fluctuations that decrease Alfvénicity and/or prevent Alfvénic fluctuations transmitting to the downstream. Consistent with shock theories, the upstreams of quasi-parallel shocks were found to be the most Alfvénic (most imbalanced and equipartitioned fluctuations). However, magnetic helicities were largely unaffected by the shock but averaged close to zero in all cases. The control of the upstream plasma beta of the occurrence of periods fulfilling Alfvénic fluctuations and flux rope criteria implies to physical processes occurring at the shock; the damping of Alfvén fluctuations in high-beta plasma and triggering of reconnection in current sheets passing through the shock. The observations < 0.5 au showed qualitatively similar results as at 1 au. The linking of found trends in turbulent properties to shock acceleration of energetic particles will be an interesting avenue of future research as energization of particle acceleration at the collisionless shocks is an ubiquitous process.

*Data availability.* The solar wind data used in this study are available from the NASA Goddard Space Flight Center Coordinated Data Analysis Web (CDAWeb; <http://cdaweb.gsfc.nasa.gov/>).

*Author contributions.* EK performed the data analysis and prepared the figures. All authors have contributed to the writing of the manuscript and interpretation of the results.

*Competing interests.* No competing interests are present.

*Acknowledgements.* We acknowledge the Finnish Centre of Excellence in Research of Sustainable Space (Research Council of Finland grant numbers 352850 and 352847). E.K. acknowledges the ERC under the European Union’s Horizon 2020 Research and Innovation Programme Project SolMAG 724391. We also acknowledge funding from the European Union’s Horizon 2020 research and innovation programme under grant agreement No. 101004159 (SERPENTINE). S.G. is supported by Research Council of Finland grants 338486 and 346612 (INERTUM). J.S. is supported by the Maili Autio Fund of the Finnish Cultural Foundation, grants 00231092 and 00242648.



## References

- Abraham-Shrauner, B. and Yun, S. H.: Interplanetary shocks seen by Ames Plasma Probe on Pioneer 6 and 7, *J. Geophys. Res.*, 81, 2097, <https://doi.org/10.1029/JA081i013p02097>, 1976.
- Adhikari, L., Zank, G. P., Hunana, P., and Hu, Q.: The Interaction of Turbulence with Parallel and Perpendicular Shocks: Theory and  
515 Observations at 1 au, *Astrophys. J.*, 833, 218, <https://doi.org/10.3847/1538-4357/833/2/218>, 2016.
- Bale, S. D., Balikhin, M. A., Horbury, T. S., Krasnoselskikh, V. V., Kucharek, H., Möbius, E., Walker, S. N., Balogh, A., Burgess, D.,  
Lembège, B., Lucek, E. A., Scholer, M., Schwartz, S. J., and Thomsen, M. F.: Quasi-perpendicular Shock Structure and Processes,  
*Space Sci. Rev.*, 118, 161–203, <https://doi.org/10.1007/s11214-005-3827-0>, 2005.
- Bavassano, B., Pietropaolo, E., and Bruno, R.: Cross-helicity and residual energy in solar wind turbulence: Radial evolution and latitudinal  
520 dependence in the region from 1 to 5 AU, *J. Geophys. Res.*, 103, 6521–6530, <https://doi.org/10.1029/97JA03029>, 1998.
- Belcher, J. W. and Davis, Leverett, J.: Large-amplitude Alfvén waves in the interplanetary medium, 2, *JGR*, 76, 3534,  
<https://doi.org/10.1029/JA076i016p03534>, 1971.
- Borovsky, J. E.: A Statistical Analysis of the Fluctuations in the Upstream and Downstream Plasmas of 109 Strong-Compression Interplan-  
etary Shocks at 1 AU, *J. Geophys. Res.*, 125, e27518, <https://doi.org/10.1029/2019JA027518>, 2020.
- 525 Bruno, R. and Carbone, V.: The Solar Wind as a Turbulence Laboratory, *Living Rev. Sol. Phys.*, 10, 2, <https://doi.org/10.12942/lrsp-2013-2>,  
2013.
- Burgess, D., Lucek, E. A., Scholer, M., Bale, S. D., Balikhin, M. A., Balogh, A., Horbury, T. S., Krasnoselskikh, V. V., Kucharek, H.,  
Lembège, B., Möbius, E., Schwartz, S. J., Thomsen, M. F., and Walker, S. N.: Quasi-parallel Shock Structure and Processes, *Space Sci.*  
*Rev.*, 118, 205–222, <https://doi.org/10.1007/s11214-005-3832-3>, 2005.
- 530 Chen, C. H. K., Bale, S. D., Salem, C. S., and Maruca, B. A.: Residual Energy Spectrum of Solar Wind Turbulence, *Astrophys. J.*, 770, 125,  
<https://doi.org/10.1088/0004-637X/770/2/125>, 2013.
- Chen, C. H. K., Bale, S. D., Bonnell, J. W., Borovikov, D., Bowen, T. A., Burgess, D., Case, A. W., Chandran, B. D. G., de Wit, T. D.,  
Goetz, K., Harvey, P. R., Kasper, J. C., Klein, K. G., Korreck, K. E., Larson, D., Livi, R., MacDowall, R. J., Malaspina, D. M., Mallet, A.,  
McManus, M. D., Moncuquet, M., Pulupa, M., Stevens, M. L., and Whittlesey, P.: The Evolution and Role of Solar Wind Turbulence in  
535 the Inner Heliosphere, *ApJS*, 246, 53, <https://doi.org/10.3847/1538-4365/ab60a3>, 2020.
- Cranmer, S. and Van Ballegoijen, A.: On the generation, propagation, and reflection of Alfvén waves from the solar photosphere to the  
distant heliosphere, *The Astrophysical Journal Supplement Series*, 156, 265, 2005.
- D’Amicis, R., Bruno, R., and Bavassano, B.: Is geomagnetic activity driven by solar wind turbulence?, *Geophys. Res. Lett.*, 34, L05108,  
<https://doi.org/10.1029/2006GL028896>, 2007.
- 540 D’Amicis, R., Bruno, R., and Bavassano, B.: Response of the geomagnetic activity to solar wind turbulence during solar cycle 23, *Journal of*  
*Atmospheric and Solar-Terrestrial Physics*, 73, 653–657, <https://doi.org/10.1016/j.jastp.2011.01.012>, 2011.
- D’Amicis, R., Bruno, R., Panasenco, O., Telloni, D., Perrone, D., Marcucci, M. F., Woodham, L., Velli, M., De Marco, R., Jagarlamudi, V.,  
Coco, I., Owen, C., Louarn, P., Livi, S., Horbury, T., André, N., Angelini, V., Evans, V., Fedorov, A., Genot, V., Lavraud, B., Matteini, L.,  
Müller, D., O’Brien, H., Pezzi, O., Rouillard, A. P., Sorriso-Valvo, L., Tenerani, A., Verscharen, D., and Zouganelis, I.: First Solar Orbiter  
545 observation of the Alfvénic slow wind and identification of its solar source, *Astron. Astrophys.*, 656, A21, <https://doi.org/10.1051/0004-6361/202140938>, 2021.



- De Keyser, J., Roth, M., De Sterck, H., and Poedts, S.: A Survey of Field-Aligned Mach Number and Plasma Beta in the Solar Wind, *Space Sci. Rev.*, 97, 201–204, <https://doi.org/10.1023/A:1011827623142>, 2001.
- Elsasser, W. M.: The Hydromagnetic Equations, *Physical Review*, 79, 183–183, <https://doi.org/10.1103/PhysRev.79.183>, 1950.
- 550 Gary, G. A.: Plasma beta above a solar active region: Rethinking the paradigm, *Solar Physics*, 203, 71–86, 2001.
- Gingell, I., Schwartz, S. J., Eastwood, J. P., Stawarz, J. E., Burch, J. L., Ergun, R. E., Fuselier, S. A., Gershman, D. J., Giles, B. L., Khotyaintsev, Y. V., Lavraud, B., Lindqvist, P. A., Paterson, W. R., Phan, T. D., Russell, C. T., Strangeway, R. J., Torbert, R. B., and Wilder, F.: Statistics of Reconnecting Current Sheets in the Transition Region of Earth’s Bow Shock, *Journal of Geophysical Research (Space Physics)*, 125, e27119, <https://doi.org/10.1029/2019JA027119>, 2020.
- 555 Gingell, I., Schwartz, S. J., Kucharek, H., Farrugia, C. J., Fryer, L. J., Plank, J., and Trattner, K. J.: Hybrid simulations of the decay of reconnected structures downstream of the bow shock, *Physics of Plasmas*, 30, 012902, <https://doi.org/10.1063/5.0129084>, 2023.
- Goldstein, M. L.: An instability of finite amplitude circularly polarized Alfvén waves, *The Astrophysical Journal*, 219, 700–704, 1978.
- Good, S. W., Hatakka, L. M., Ala-Lahti, M., Soljento, J. E., Osmane, A., and Kilpua, E. K. J.: Cross helicity of interplanetary coronal mass ejections at 1 au, *Mon. Not. R. Astron. Soc.*, 514, 2425–2433, <https://doi.org/10.1093/mnras/stac1388>, 2022.
- 560 Good, S. W., Rantala, O. K., Jylhä, A. S. M., Chen, C. H. K., Möstl, C., and Kilpua, E. K. J.: Turbulence Properties of Interplanetary Coronal Mass Ejections in the Inner Heliosphere: Dependence on Proton Beta and Flux Rope Structure, *arXiv e-prints*, arXiv:2307.09800, <https://doi.org/10.48550/arXiv.2307.09800>, 2023.
- Hadid, L. Z., Sahraoui, F., Kiyani, K. H., Retinò, A., Modolo, R., Canu, P., Masters, A., and Dougherty, M. K.: Nature of the MHD and Kinetic Scale Turbulence in the Magnetosheath of Saturn: Cassini Observations, *Astrophys. J.*, 813, L29, [https://doi.org/10.1088/2041-](https://doi.org/10.1088/2041-8205/813/2/L29)
- 565 [8205/813/2/L29](https://doi.org/10.1088/2041-8205/813/2/L29), 2015.
- Hollweg, J. V.: Nonlinear Landau Damping of Alfvén Waves, *PRL*, 27, 1349–1352, <https://doi.org/10.1103/PhysRevLett.27.1349>, 1971.
- Horbury, T. S., O’Brien, H., Carrasco Blazquez, I., Bendyk, M., Brown, P., Hudson, R., Evans, V., Oddy, T. M., Carr, C. M., Beek, T. J., Cupido, E., Bhattacharya, S., Dominguez, J. A., Matthews, L., Myklebust, V. R., Whiteside, B., Bale, S. D., Baumjohann, W., Burgess, D., Carbone, V., Cargill, P., Eastwood, J., Erdös, G., Fletcher, L., Forsyth, R., Giacalone, J., Glassmeier, K. H., Goldstein, M. L., Hoeksema,
- 570 T., Lockwood, M., Magnes, W., Maksimovic, M., Marsch, E., Matthaeus, W. H., Murphy, N., Nakariakov, V. M., Owen, C. J., Owens, M., Rodriguez-Pacheco, J., Richter, I., Riley, P., Russell, C. T., Schwartz, S., Vainio, R., Velli, M., Vennerstrom, S., Walsh, R., Wimmer-Schweingruber, R. F., Zank, G., Müller, D., Zouganelis, I., and Walsh, A. P.: The Solar Orbiter magnetometer, *Astron. Astrophys.*, 642, A9, <https://doi.org/10.1051/0004-6361/201937257>, 2020.
- Huang, S. Y., Hadid, L. Z., Sahraoui, F., Yuan, Z. G., and Deng, X. H.: On the Existence of the Kolmogorov Inertial Range in the Terrestrial
- 575 *Magnetosheath Turbulence*, *Astrophys. J. Lett.*, 836, L10, <https://doi.org/10.3847/2041-8213/836/1/L10>, 2017.
- Huang, S. Y., Wang, Q. Y., Sahraoui, F., Yuan, Z. G., Liu, Y. J., Deng, X. H., Sun, W. J., Jiang, K., Xu, S. B., Yu, X. D., Wei, Y. Y., and Zhang, J.: Analysis of Turbulence Properties in the Mercury Plasma Environment Using MESSENGER Observations, *Astrophys. J.*, 891, 159, <https://doi.org/10.3847/1538-4357/ab7349>, 2020.
- Jian, L., Russell, C. T., Luhmann, J. G., and Skoug, R. M.: Properties of Stream Interactions at One AU During 1995–2004, *SoPh*, 239,
- 580 [337–392](https://doi.org/10.1007/s11207-006-0132-3), <https://doi.org/10.1007/s11207-006-0132-3>, 2006.
- Kilpua, E., Koskinen, H. E. J., and Pulkkinen, T. I.: Coronal mass ejections and their sheath regions in interplanetary space, *Living Reviews in Solar Physics*, 14, 5, <https://doi.org/10.1007/s41116-017-0009-6>, 2017.



- Kilpua, E., Vainio, R., Cohen, C., Dresing, N., Good, S., Ruohotie, J., Trotta, D., Bale, S. D., Christian, E., Hill, M., McComas, D. J., McNutt, R., and Schwadron, N.: Energetic ion enhancements in sheaths driven by interplanetary coronal mass ejections, *Astrophys. Space Sci.*, 585 368, 66, <https://doi.org/10.1007/s10509-023-04201-6>, 2023.
- Kilpua, E. K. J., Lumme, E., Andreeva, K., Isavnin, A., and Koskinen, H. E. J.: Properties and drivers of fast interplanetary shocks near the orbit of the Earth (1995–2013), *J. Geophys. Res.*, 120, 4112–4125, <https://doi.org/10.1002/2015JA021138>, 2015.
- Kilpua, E. K. J., Good, S. W., Ala-Lahti, M., Osmane, A., Fontaine, D., Hadid, L., Janvier, M., and Yordanova, E.: Statistical analysis of magnetic field fluctuations in CME-driven sheath regions, *Frontiers in Astronomy and Space Sciences*, 7, 109, 590 <https://doi.org/10.3389/fspas.2020.610278>, 2021.
- Lee, M. A.: Coupled hydromagnetic wave excitation and ion acceleration upstream of the earth’s bow shock, *J. Geophys. Res.*, 87, 5063–5080, <https://doi.org/10.1029/JA087iA07p05063>, 1982.
- Lepping, R. P., Acuña, M. H., Burlaga, L. F., Farrell, W. M., Slavin, J. A., Schatten, K. H., Mariani, F., Ness, N. F., Neubauer, F. M., Whang, Y. C., Byrnes, J. B., Kennon, R. S., Panetta, P. V., Scheifele, J., and Worley, E. M.: The Wind Magnetic Field Investigation, *Space Sci. Rev.*, 71, 207–229, <https://doi.org/10.1007/BF00751330>, 1995. 595
- Lin, R. P., Anderson, K. A., Ashford, S., Carlson, C., Curtis, D., Ergun, R., Larson, D., McFadden, J., McCarthy, M., Parks, G. K., Rème, H., Bosqued, J. M., Coutelier, J., Cotin, F., D’Uston, C., Wenzel, K. P., Sanderson, T. R., Henrion, J., Ronnet, J. C., and Paschmann, G.: A Three-Dimensional Plasma and Energetic Particle Investigation for the Wind Spacecraft, *Space Sci. Rev.*, 71, 125–153, <https://doi.org/10.1007/BF00751328>, 1995.
- 600 Mattheaus, W. H. and Goldstein, M. L.: Measurement of the rugged invariants of magnetohydrodynamic turbulence in the solar wind, *J. Geophys. Res.*, 87, 6011–6028, <https://doi.org/10.1029/JA087iA08p06011>, 1982.
- Mullan, D. J. and Smith, C. W.: Solar Wind Statistics at 1 AU: Alfvén Speed and Plasma Beta, *Sol. Phys.*, 234, 325–338, <https://doi.org/10.1007/s11207-006-2077-y>, 2006.
- Müller, D., St. Cyr, O. C., Zouganelis, I., Gilbert, H. R., Marsden, R., Nieves-Chinchilla, T., Antonucci, E., Auchère, F., Berghmans, D., 605 Horbury, T. S., Howard, R. A., Krucker, S., Maksimovic, M., Owen, C. J., Rochus, P., Rodriguez-Pacheco, J., Romoli, M., Solanki, S. K., Bruno, R., Carlsson, M., Fludra, A., Harra, L., Hassler, D. M., Livi, S., Louarn, P., Peter, H., Schühle, U., Teriaca, L., del Toro Iniesta, J. C., Wimmer-Schweingruber, R. F., Marsch, E., Velli, M., De Groof, A., Walsh, A., and Williams, D.: The Solar Orbiter mission. Science overview, *Astron. Astrophys.*, 642, A1, <https://doi.org/10.1051/0004-6361/202038467>, 2020.
- Nakanotani, M., Zank, G. P., and Zhao, L. L.: Interaction between Multiple Current Sheets and a Shock Wave: 2D Hybrid Kinetic Simulations, 610 *Astrophys. J.*, 922, 219, <https://doi.org/10.3847/1538-4357/ac2e06>, 2021.
- Odstrčil, D. and Karlický, M.: Triggering of magnetic reconnection in the current sheet by shock waves., *Astron. Astrophys.*, 326, 1252–1258, 1997.
- Ogilvie, K. W. and Desch, M. D.: The wind spacecraft and its early scientific results, *Adv. Space Res.*, 20, 559–568, [https://doi.org/10.1016/S0273-1177\(97\)00439-0](https://doi.org/10.1016/S0273-1177(97)00439-0), 1997.
- 615 Owen, C. J., Bruno, R., Livi, S., Louarn, P., Al Janabi, K., Allegrini, F., Amoros, C., Baruah, R., Barthe, A., Berthomier, M., Bordon, S., Brockley-Blatt, C., Brysbaert, C., Capuano, G., Collier, M., DeMarco, R., Fedorov, A., Ford, J., Fortunato, V., Fratter, I., Galvin, A. B., Hancock, B., Heitzler, D., Kataria, D., Kistler, L., Lepri, S. T., Lewis, G., Loeffler, C., Marty, W., Mathon, R., Mayall, A., Mele, G., Ogasawara, K., Orlandi, M., Pacros, A., Penou, E., Persyn, S., Petiot, M., Phillips, M., Přeč, L., Raines, J. M., Reden, M., Rouillard, A. P., Rousseau, A., Rubiella, J., Seran, H., Spencer, A., Thomas, J. W., Trevino, J., Verscharen, D., Wurz, P., Alapide, A., Amoroso, 620 L., André, N., Anekallu, C., Arciuli, V., Arnett, K. L., Ascolese, R., Bancroft, C., Bland, P., Brysch, M., Calvanese, R., Castronuovo,



- M., Čermák, I., Chornay, D., Clemens, S., Coker, J., Collinson, G., D'Amicis, R., Dandouras, I., Darnley, R., Davies, D., Davison, G., De Los Santos, A., Devoto, P., Dirks, G., Edlund, E., Fazakerley, A., Ferris, M., Frost, C., Fruit, G., Garat, C., Génot, V., Gibson, W., Gilbert, J. A., de Giosa, V., Gradone, S., Hailey, M., Horbury, T. S., Hunt, T., Jacquy, C., Johnson, M., Lavraud, B., Lawrenson, A., Leblanc, F., Lockhart, W., Maksimovic, M., Malpus, A., Marcucci, F., Mazelle, C., Monti, F., Myers, S., Nguyen, T., Rodriguez-Pacheco, J., Phillips, I., Popecki, M., Rees, K., Rogacki, S. A., Ruane, K., Rust, D., Salatti, M., Sauvaud, J. A., Stakhiv, M. O., Stange, J., Stubbs, T., Taylor, T., Techer, J. D., Terrier, G., Thibodeaux, R., Urdiales, C., Varsani, A., Walsh, A. P., Watson, G., Wheeler, P., Willis, G., Wimmer-Schweingruber, R. F., Winter, B., Yardley, J., and Zouganelis, I.: The Solar Orbiter Solar Wind Analyser (SWA) suite, *Astron. Astrophys.*, 642, A16, <https://doi.org/10.1051/0004-6361/201937259>, 2020.
- 625 Park, B., Pitňa, A., Šafránková, J., Němeček, Z., Krupařová, O., Krupař, V., Zhao, L., and Silwal, A.: Change of Spectral Properties of Magnetic Field Fluctuations across Different Types of Interplanetary Shocks, *Astrophys. J.*, 954, L51, <https://doi.org/10.3847/2041-8213/acf4ff>, 2023.
- Parker, E. N.: Dynamics of the Interplanetary Gas and Magnetic Fields., *Astrophys. J.*, 128, 664, <https://doi.org/10.1086/146579>, 1958.
- Perri, S. and Balogh, A.: Differences in solar wind cross-helicity and residual energy during the last two solar minima, *Geophys. Res. Lett.*, 37, L17102, <https://doi.org/10.1029/2010GL044570>, 2010.
- 635 Pitňa, A., Šafránková, J., Němeček, Z., Goncharov, O., Němec, F., Přeč, L., Chen, C. H. K., and Zastenker, G. N.: Density Fluctuations Upstream and Downstream of Interplanetary Shocks, *Astrophys. J.*, 819, 41, <https://doi.org/10.3847/0004-637X/819/1/41>, 2016.
- Pitňa, A., Šafránková, J., Němeček, Z., Ďurovcová, T., and Kis, A.: Turbulence Upstream and Downstream of Interplanetary Shocks, *Frontiers in Physics*, 8, 654, <https://doi.org/10.3389/fphy.2020.626768>, 2021.
- Richardson, I. G.: Solar wind stream interaction regions throughout the heliosphere, *Living Reviews in Solar Physics*, 15, 1, <https://doi.org/10.1007/s41116-017-0011-z>, 2018.
- 640 Roberts, D. A., Klein, L. W., Goldstein, M. L., and Matthaeus, W. H.: The nature and evolution of magnetohydrodynamic fluctuations in the solar wind: Voyager observations, *J. Geophys. Res.*, 92, 11 021–11 040, <https://doi.org/10.1029/JA092iA10p11021>, 1987.
- Ruohotie, J., Kilpua, E. K. J., Good, S. W., and Ala-Lahti, M.: Small-scale flux ropes in ICME sheaths, *Frontiers in Astronomy and Space Sciences*, 9, 943247, <https://doi.org/10.3389/fspas.2022.943247>, 2022.
- 645 Sishtla, C. P., Pomoell, J., Kilpua, E., Good, S., Daei, F., and Palmroth, M.: Flux-tube-dependent propagation of Alfvén waves in the solar corona, *Astron. Astrophys.*, 661, A58, <https://doi.org/10.1051/0004-6361/202142999>, 2022.
- Sishtla, C. P., Pomoell, J., Vainio, R., Kilpua, E., and Good, S.: Modelling the interaction of Alfvénic fluctuations with coronal mass ejections in the low solar corona, *Astron. Astrophys.*, 679, A54, <https://doi.org/10.1051/0004-6361/202347250>, 2023.
- Smith, C. W.: Magnetic helicity in the solar wind, *Advances in Space Research*, 32, 1971–1980, [https://doi.org/10.1016/S0273-1177\(03\)90635-1](https://doi.org/10.1016/S0273-1177(03)90635-1), 2003.
- 650 Snekvik, K., Tanskanen, E. I., and Kilpua, E. K. J.: An automated identification method for Alfvénic streams and their geoeffectiveness, *J. Geophys. Res.*, 118, 5986–5998, <https://doi.org/10.1002/jgra.50588>, 2013.
- Soljento, J. E., Good, S. W., Osmane, A., and Kilpua, E. K. J.: Imbalanced Turbulence Modified by Large-scale Velocity Shears in the Solar Wind, *Astrophys. J.*, 946, L19, <https://doi.org/10.3847/2041-8213/acc071>, 2023.
- 655 Squire, J., Schekochihin, A. A., and Quataert, E.: Amplitude limits and nonlinear damping of shear-Alfvén waves in high-beta low-collisionality plasmas, *New Journal of Physics*, 19, 055005, <https://doi.org/10.1088/1367-2630/aa6bb1>, 2017.
- Tomczyk, S. and McIntosh, S. W.: Time-Distance Seismology of the Solar Corona with CoMP, *Astrophys. J.*, 697, 1384–1391, <https://doi.org/10.1088/0004-637X/697/2/1384>, 2009.



- Trotta, D., Pecora, F., Settino, A., Perrone, D., Hietala, H., Horbury, T., Matthaeus, W., Burgess, D., Servidio, S., and Valentini, F.: On the  
660 Transmission of Turbulent Structures across the Earth's Bow Shock, *The Astrophysical Journal*, 933, 167, <https://doi.org/10.3847/1538-4357/ac7798>, 2022.
- Trotta, D., Vuorinen, L., Hietala, H., Horbury, T., Dresing, N., Gieseler, J., Kouloumvakos, A., Price, D., Valentini, F., Kilpua, E., and Vainio, R.: Single-spacecraft techniques for shock parameters estimation: A systematic approach, *Frontiers in Astronomy and Space Sciences*, 9, 1005672, <https://doi.org/10.3389/fspas.2022.1005672>, 2022.
- 665 Trotta, D., Pezzi, O., Burgess, D., Preisser, L., Blanco-Cano, X., Kajdic, P., Hietala, H., Horbury, T. S., Vainio, R., Dresing, N., Retinò, A., Marcucci, M. F., Sorriso-Valvo, L., Servidio, S., and Valentini, F.: Three-dimensional modelling of the shock-turbulence interaction, *Monthly Notices of the Royal Astronomical Society*, 525, 1856–1866, <https://doi.org/10.1093/mnras/stad2384>, 2023.
- Trotta, D., Hietala, H., Dresing, N., Horbury, T., Kartavykh, Y., Gieseler, J., Jebaraj, I., Gómez-Herrero, R., Espinosa Lara, L., and Vainio, R.: Solar Orbiter Cycle 25 Interplanetary Shock List (Dataset), Zenodo, 2024a.
- 670 Trotta, D., Larosa, A., Nicolaou, G., Horbury, T. S., Matteini, L., Hietala, H., Blanco-Cano, X., Franci, L., Chen, C. H. K., Zhao, L., Zank, G. P., Cohen, C. M. S., Bale, S. D., Laker, R., Fargette, N., Valentini, F., Khotyaintsev, Y., Kieokaew, R., Raouafi, N., Davies, E., Vainio, R., Dresing, N., Kilpua, E., Karlsson, T., Owen, C. J., and Wimmer-Schweingruber, R. F.: Properties of an Interplanetary Shock Observed at 0.07 and 0.7 au by Parker Solar Probe and Solar Orbiter, *Astrophys. J.*, 962, 147, <https://doi.org/10.3847/1538-4357/ad187d>, 2024b.
- Tu, C. Y. and Marsch, E.: Magnetohydrodynamic Structures Waves and Turbulence in the Solar Wind - Observations and Theories, *Space*  
675 *Sci. Rev.*, 73, 1–210, <https://doi.org/10.1007/BF00748891>, 1995.
- Vainio, R. and Schlickeiser, R.: Alfvén wave transmission and particle acceleration in parallel shock waves, *Astron. Astrophys.*, 331, 793–799, 1998.
- Vainio, R. and Schlickeiser, R.: Self-consistent Alfvén-wave transmission and test-particle acceleration at parallel shocks, *Astron. Astrophys.*, 343, 303–311, 1999.
- 680 Vainio, R. and Spanier, F.: Evolution of Alfvén waves by three-wave interactions in super-Alfvénic shocks, *Astron. Astrophys.*, 437, 1–8, <https://doi.org/10.1051/0004-6361:20042433>, 2005.
- Verscharen, D., Klein, K. G., and Maruca, B. A.: The multi-scale nature of the solar wind, *Living Rev. Sol. Phys.*, 16, 5, <https://doi.org/10.1007/s41116-019-0021-0>, 2019.
- Völk, H. J. and Cesarsky, C. J.: Nonlinear Landau damping of Alfvén waves in a high beta plasma., *Zeitschrift Naturforschung Teil A*, 37,  
685 809–815, <https://doi.org/10.1515/zna-1982-0814>, 1982.
- Zank, G. P., Nakanotani, M., Zhao, L. L., Du, S., Adhikari, L., Che, H., and le Roux, J. A.: Flux Ropes, Turbulence, and Collisionless Perpendicular Shock Waves: High Plasma Beta Case, , 913, 127, <https://doi.org/10.3847/1538-4357/abf7c8>, 2021.
- Zhao, L. L., Zank, G. P., He, J. S., Telloni, D., Hu, Q., Li, G., Nakanotani, M., Adhikari, L., Kilpua, E. K. J., Horbury, T. S., O'Brien, H., Evans, V., and Angelini, V.: Turbulence and wave transmission at an ICME-driven shock observed by the Solar Orbiter and Wind, *Astron. Astrophys.*, 656, A3, <https://doi.org/10.1051/0004-6361/202140450>, 2021.
- 690 Zheng, J. and Hu, Q.: Observational Evidence for Self-generation of Small-scale Magnetic Flux Ropes from Intermittent Solar Wind Turbulence, *Astrophys. J. Lett.*, 852, L23, <https://doi.org/10.3847/2041-8213/aaa3d7>, 2018.



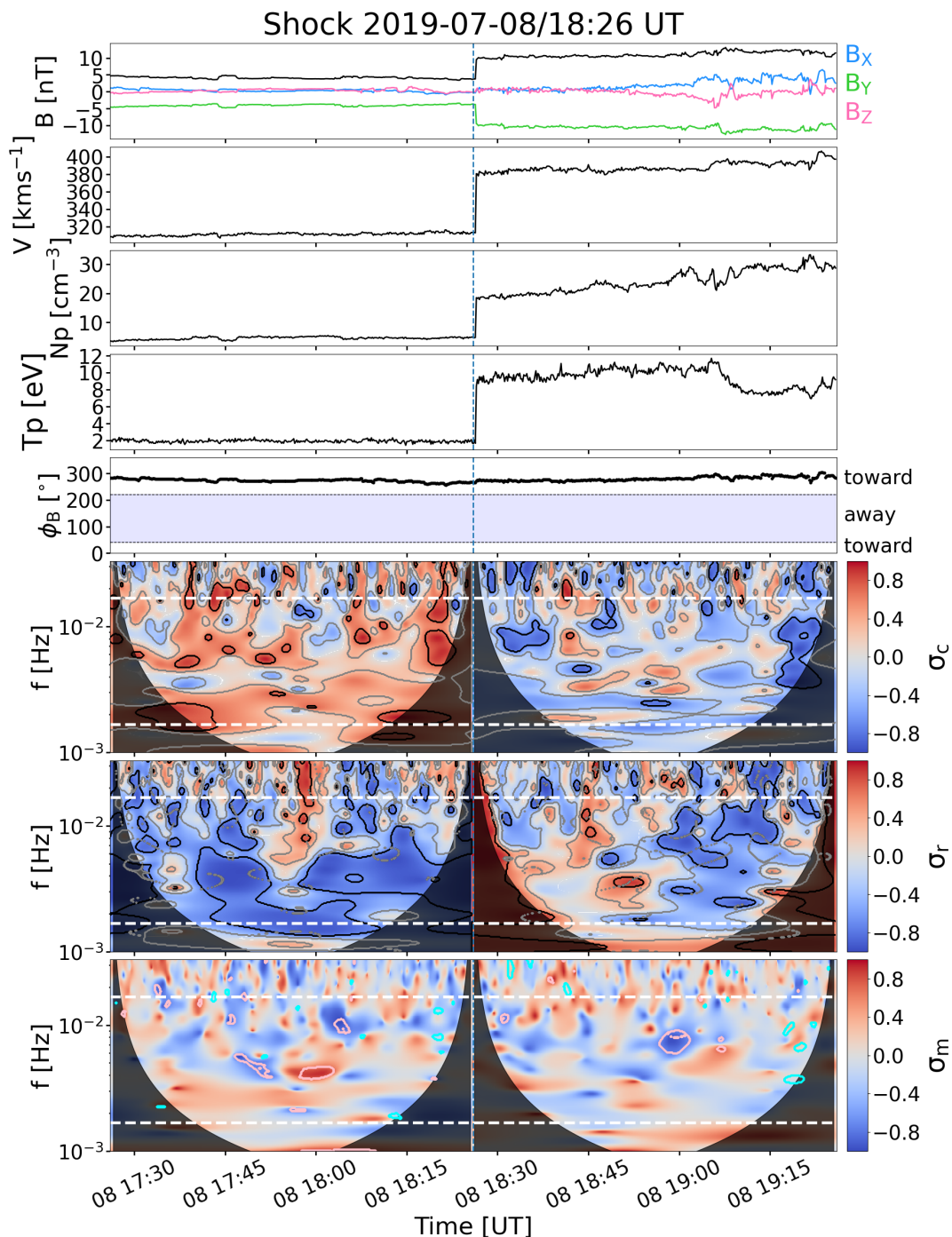


**Figure 1.** A shock observed by *Wind* on 8 July 2019. From top to bottom, the first five panels show: the magnetic field magnitude and the GSE components; solar wind speed; density; temperature; and IMF clock angle. The bottom three panels show wavelet spectrograms of normalised cross-helicity, residual energy and magnetic helicity. Dashed white lines show the frequencies limiting the high frequencies / small scales (16.7 mHz / 1 min) and low frequencies / large scales (1.67 mHz / 10 min) used in the analysis. Black contours in the spectrograms delineate where absolute values of parameters exceed 0.7, and grey contours outline  $|\sigma_r| > 0.3$  and  $|\sigma_c| > 0.3$  regions. The pink and cyan contours in the bottom panel outline the intervals that fulfil the criteria for Alfvénic fluctuations and flux ropes imposed on  $\sigma_c$ ,  $\sigma_r$ , and  $\sigma_m$ , see Section 3.3.3 for details.

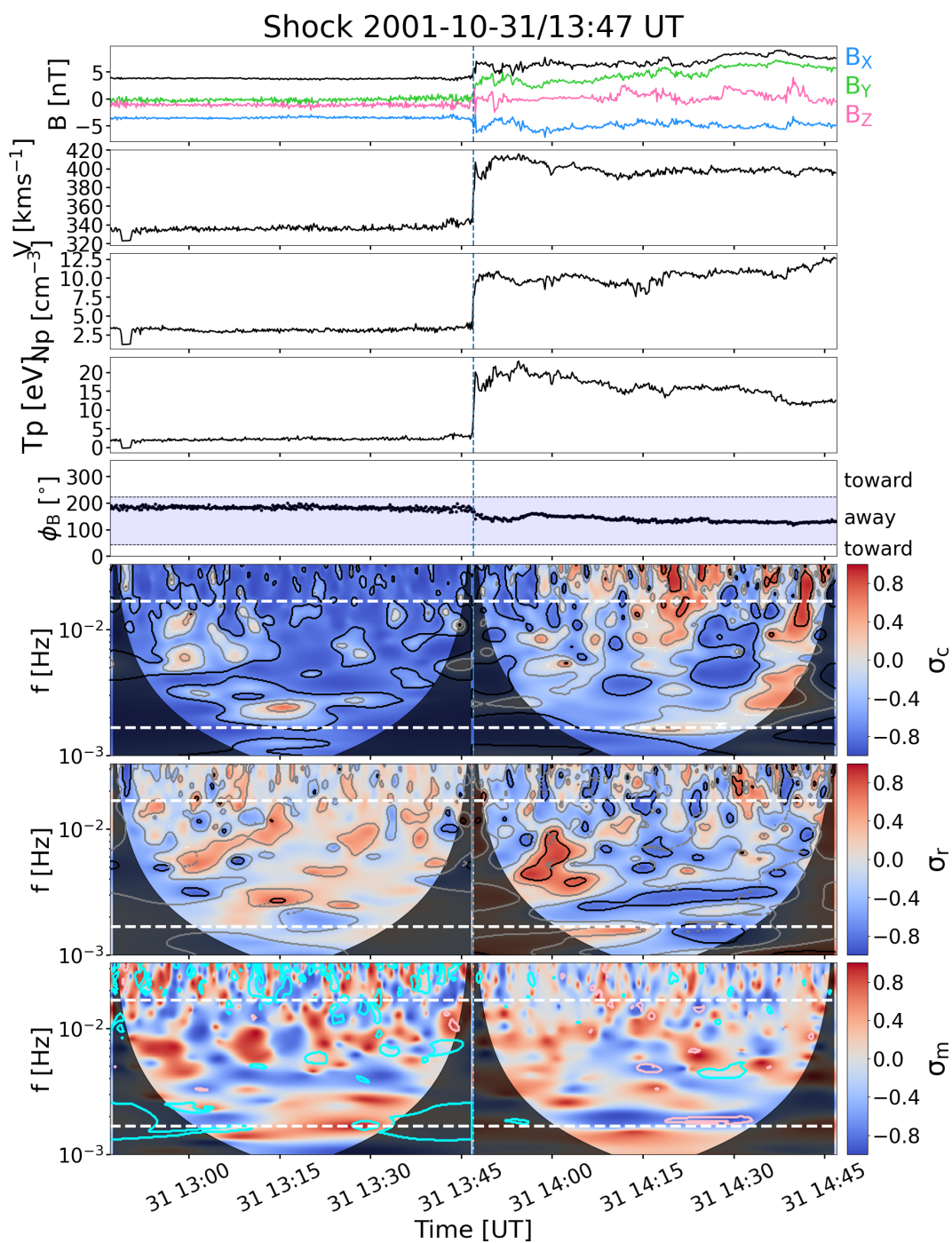


**Figure 2.** A shock observed by *Wind* on 31 October 2001. The panels are the same as in Figure 1.

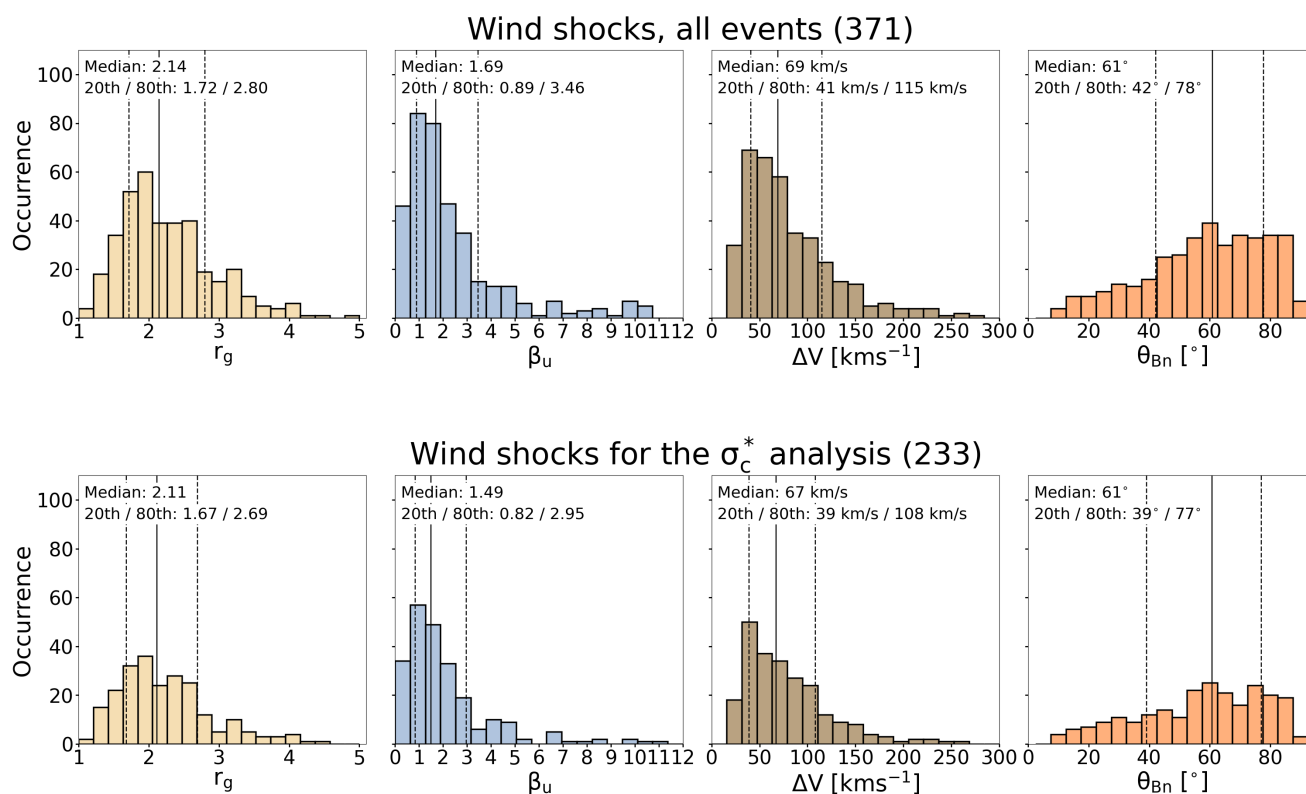


**Figure 3.** Histograms of parameters for interplanetary shocks detected by the *Wind* spacecraft during 1995 – 2023. The dashed grey lines show the 20th and 80th percentiles. The top row shows the distribution for all *Wind* shocks and the bottom row shows the distribution for those used in the  $\sigma_c^*$  analysis. From left to right, the panels show the distributions for the shock gas compression ratio, upstream plasma beta, velocity jump across the shock, and shock angle.

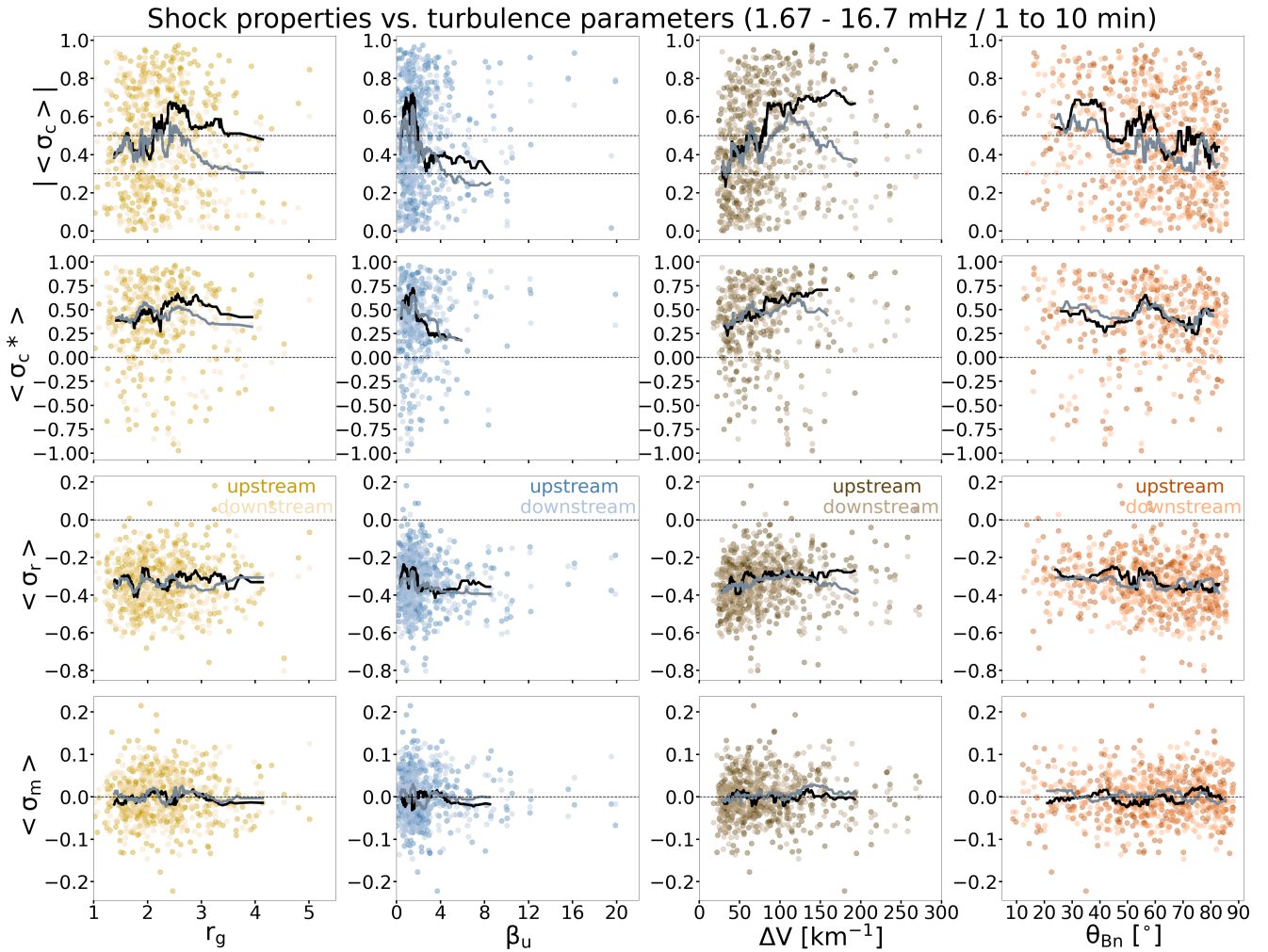


**Figure 4.** The top row shows the absolute values of the 1-hour averages of the normalised cross-helicity ( $|\langle \sigma_c \rangle|$ ). The next rows show the 1-hour averages of the rectified cross-helicity ( $\langle \sigma_c^* \rangle$ ), residual energy ( $\langle \sigma_r \rangle$ ) and magnetic helicity ( $\langle \sigma_m \rangle$ ). The values are shown both for the upstream (darker colours) and downstream (lighter colours) as a function of shock gas compression ratio ( $r_g$ ), upstream plasma beta ( $\beta_u$ ), velocity jump at the shock ( $\Delta V$ ), and shock angle ( $\theta_{Bn}$ ). Curves give the 40-event running median for the upstream (black) and downstream (grey).

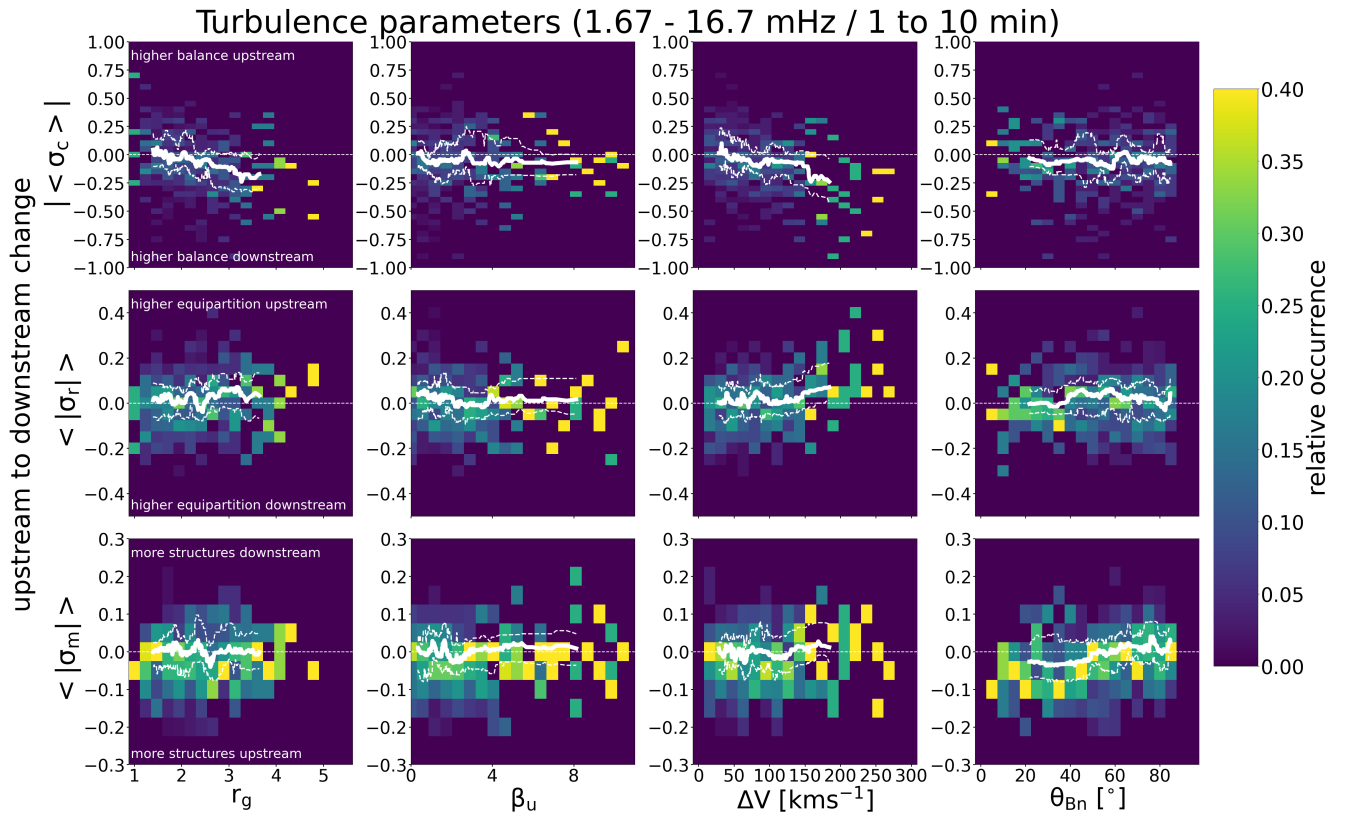


**Figure 5.** Heatmaps of the relative occurrence organised with the shock parameters and change from the upstream to downstream absolute values of the 1-hr averaged cross-helicity ( $|\langle \sigma_c \rangle|$ ), and the 1-hour averaged absolute values of residual energy ( $|\langle \sigma_r \rangle|$ ) and magnetic helicity ( $|\langle \sigma_m \rangle|$ ). (see the text for details). The white curves give the 40-event running medians of the change. The dashed white curves give the corresponding upper and lower quartiles





## PDFs separated by Gas Ratio and Upstream Beta

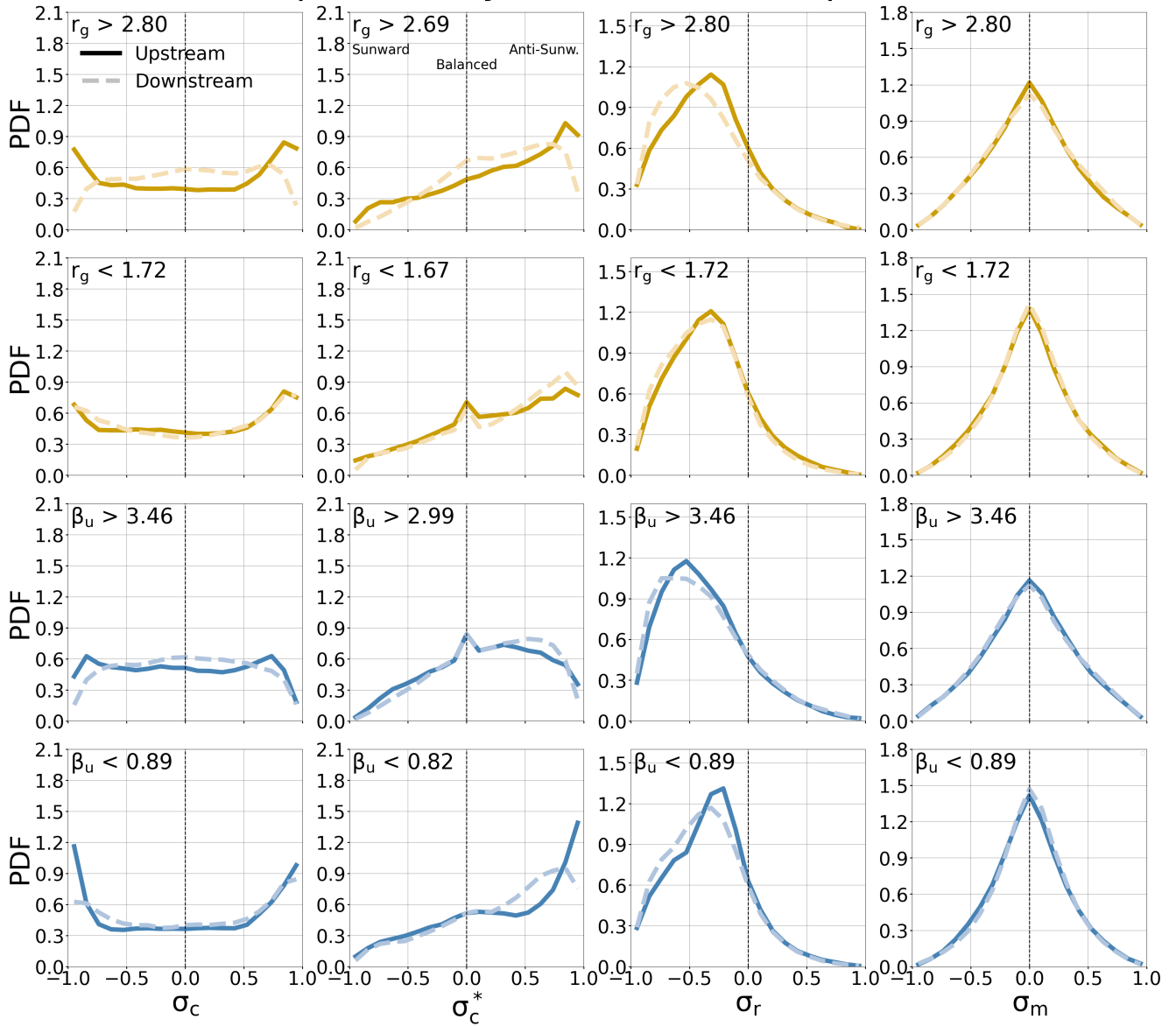


**Figure 6.** PDFs for shocks separated into two subsets using the 80th and 20th quartiles of the shock gas compression ratio and the upstream plasma beta for cross-helicity ( $\sigma_c$ ), rectified cross-helicity ( $\sigma_c^*$ ), residual energy ( $\sigma_r$ ) and magnetic helicity ( $\sigma_m$ ).





## PDFs separated by Speed Jump and Shock Angle

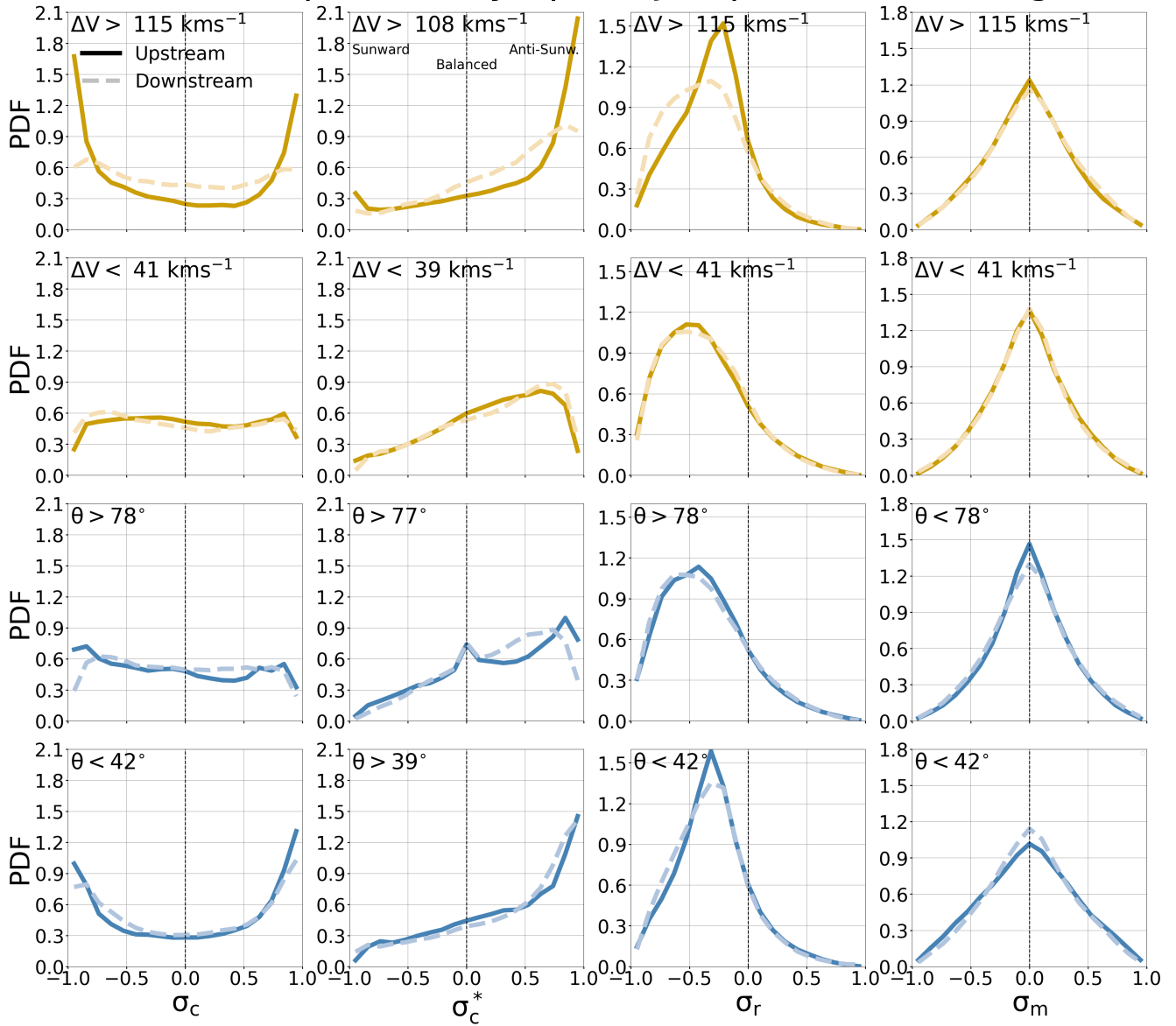


**Figure 7.** Probability distribution functions (PDFs) for shocks separated into two subsets using the 80th and 20th quartiles of the shock speed jump and shock angle for cross-helicity ( $\sigma_c$ ), rectified cross-helicity ( $\sigma_c^*$ ), residual energy ( $\sigma_r$ ) and magnetic helicity ( $\sigma_m$ ).

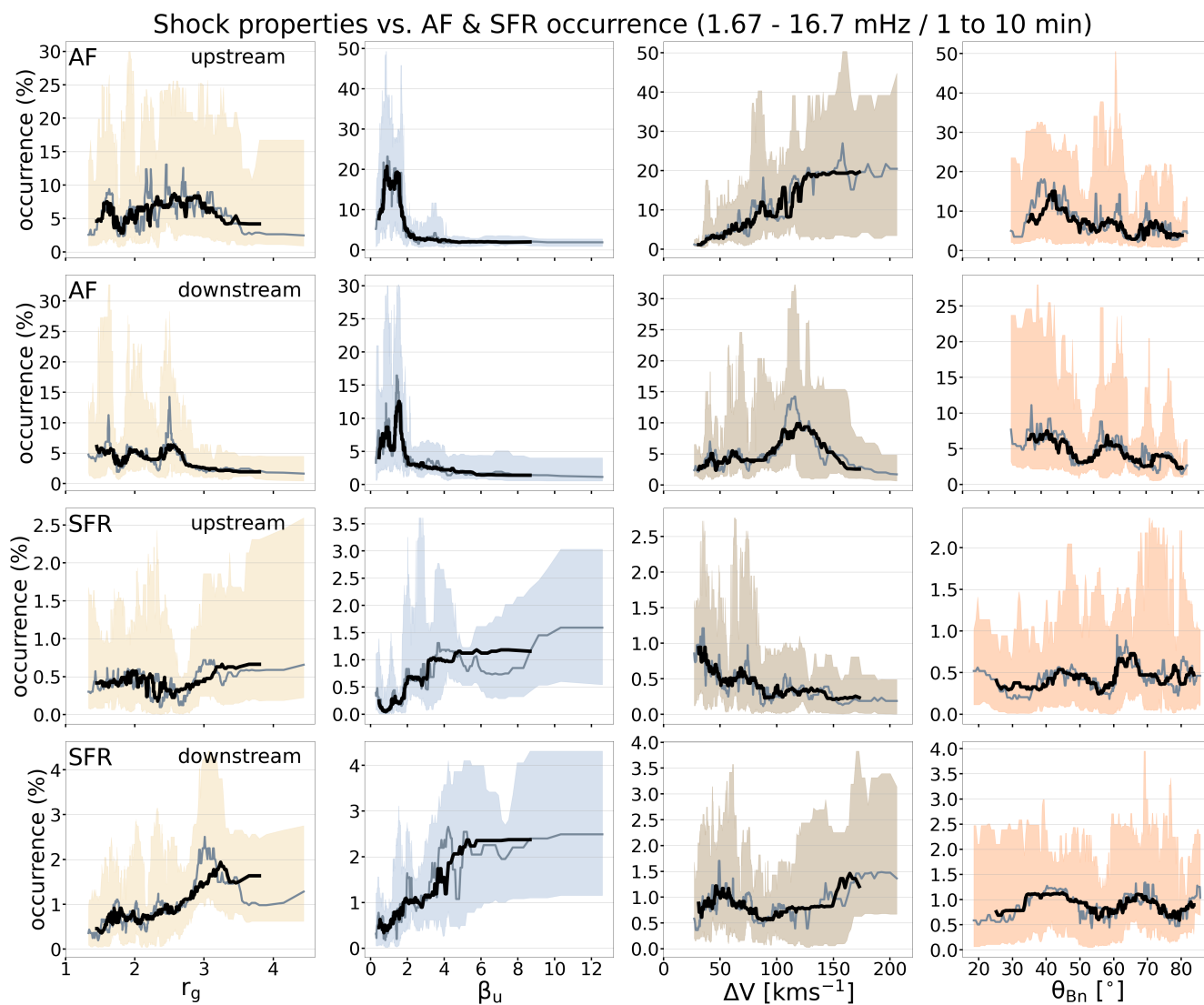


**Figure 8.** The 30-event (grey) and 60-event (black) running medians of the occurrence percentage of periods that fulfil the AF and FR criteria (see the text for details) in the shock upstream and downstream as a function of the selected shock parameters. Shading shows the interquartile range for the 30-event running medians.

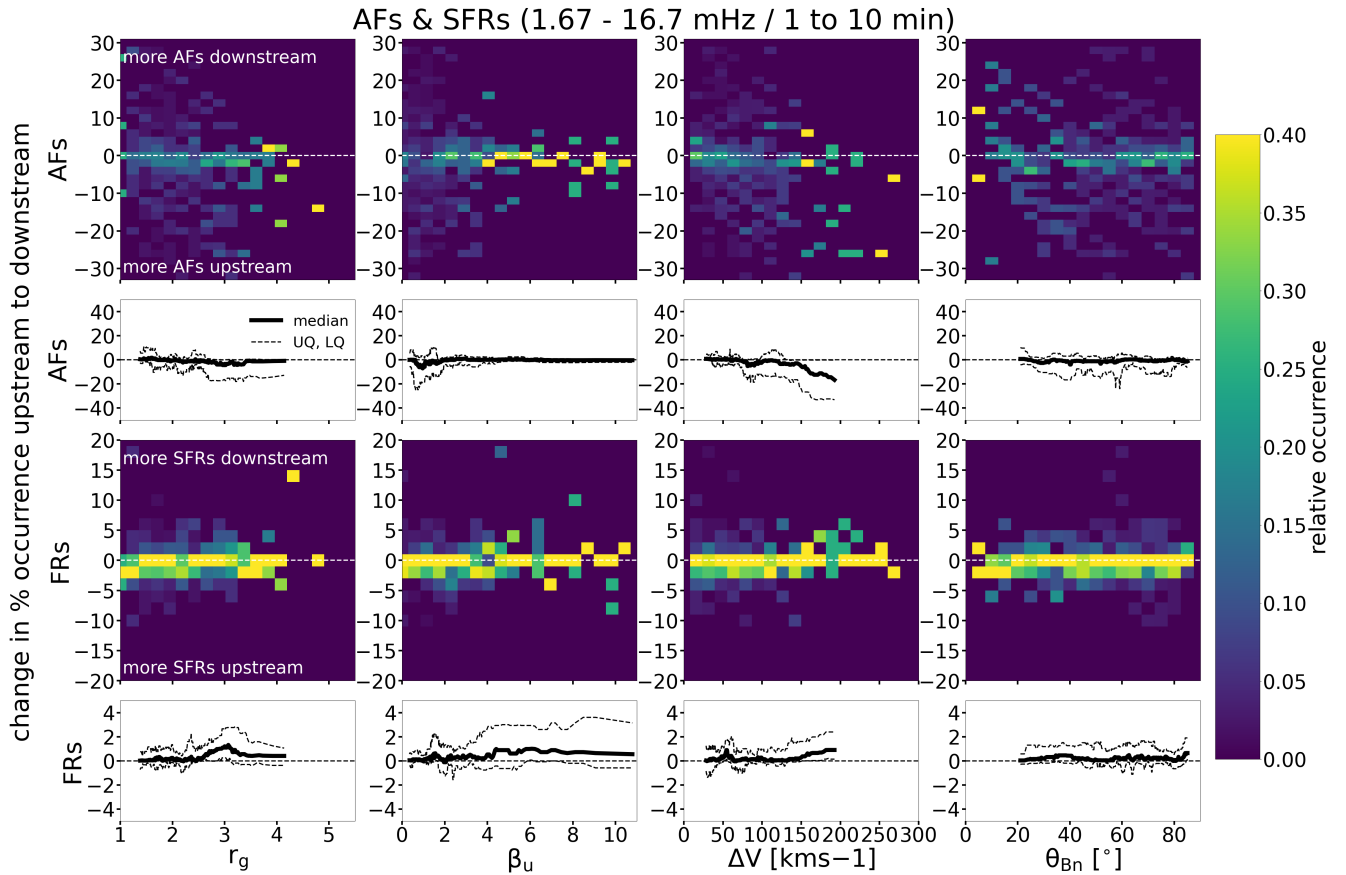


**Figure 9.** Heatmaps of the relative occurrence rates as a function of the shock parameters and change across the shock in the percentage AF and FR periods, see the text for details. The white curves give the 40-event running medians and upper and lower quartiles of the change.

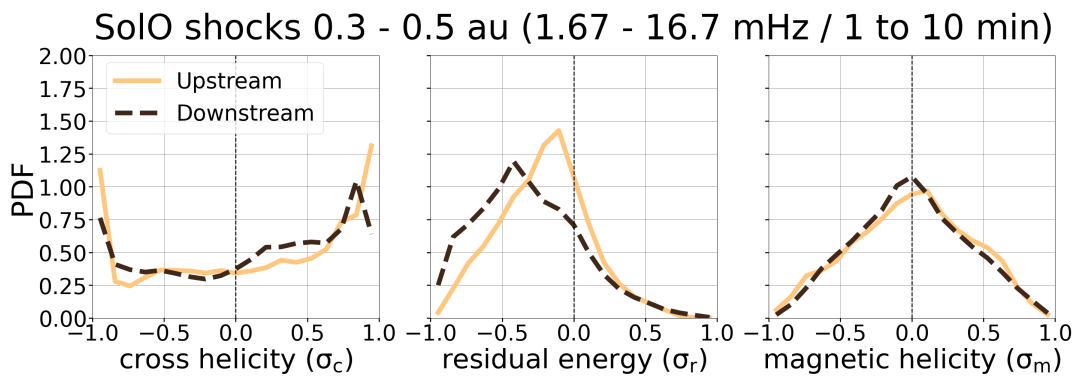


**Figure 10.** PDFs of cross-helicity, residual energy and magnetic helicity for seven *Solar Orbiter* shocks that were observed below 0.5 au.

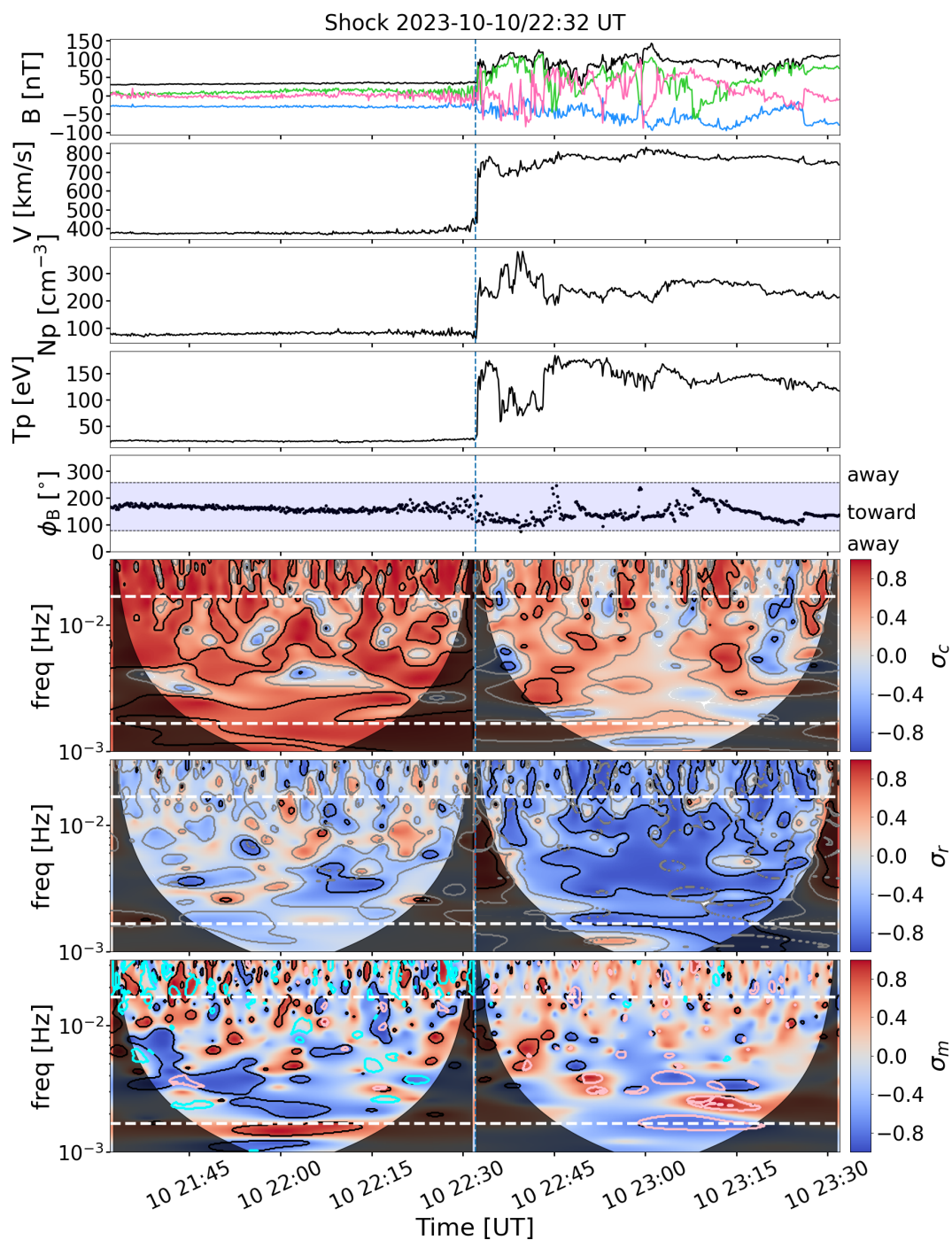


**Figure 11.** A shock observed by *Solar Orbiter* on 10 October 2023. The panels are same as in Figure 1.